ACS APPLIED MATERIALS & INTERFACES

www.acsami.org

Research Article

Controllability of the Conductive Filament in Porous SiO_x Memristors by Humidity-Mediated Silver Ion Migration

Haoze Li, Qin Gao, Juan Gao, Jiangshun Huang, Xueli Geng, Guoxing Wang, Bo Liang, Xinghe Li, Mei Wang, Zhisong Xiao, Paul K. Chu, and Anping Huang*

Cite This: *ACS Appl. Mater. Interfaces* 2023, 15, 46449−46459

Read Online

ACCESS | Metrics & More | Article Recommendations | Supporting Information

ABSTRACT: Oxide-based memristors composed of Ag/porous SiO_x/Si stacks are fabricated using different etching time durations between 0 and 90 s, and the memristive properties are analyzed in the relative humidity (RH) range of 30−60%. The combination of humidity and porous structure provides binding sites to control silver filament formation with a confined nanoscale channel. The memristive properties of devices show high on/off ratios up to 10^8 and a dispersion coefficient of 0.1% of the high resistance state (C_{HRS}) when the RH increases to 60%. Humidity-mediated silver ion migration in the porous SiO_x memristors is investigated, and the mechanism leading to the synergistic effects between the porous structure and environmental humidity is elucidated. The artificial neural network constructed theoretically shows that the recognition rate increases from 60.9 to 85.29% in the RH range of 30−60%. The results and theoretical understanding provide insights into the design and optimization of oxide-based memristors in neuromorphic computing applications.

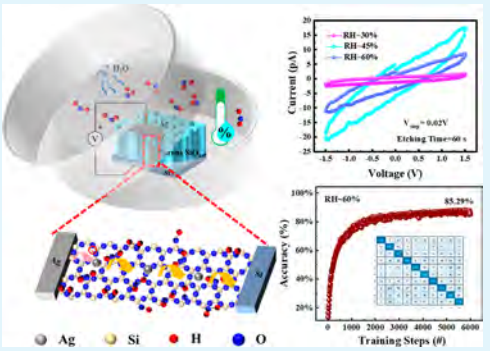

KEYWORDS: *memristors, porous silicon oxide, relative humidity, filament, neuromorphic computing*

INTRODUCTION

Oxide-based memristors have large potential in future neuromorphic devices due to their simple structure, fast switching speed, and compatibility with complementary metal oxide semiconductor processing.[1,2] Generally, the properties of oxide-based memristors mainly depend on resistance switching between the two conductors from the high-resistance state (HRS) to the low-resistance state (LRS) under electrical control.[3,4] The switching effects in oxide-based memristors are attributable to the nanoscale conductive filaments (CF), which are formed/annihilated by controlling the thermal or external electric field generation.[5,6] The memristive switching mechanism relies on electrochemical effects and nanoionic processes involving dissolution of metal atoms from an electrochemically active electrode. The resulting migration of metal ions in an insulating matrix forms a metallic conductive bridge that is responsible for the change of the device resistance.[7] Wu et al. have revealed the formation of CF in HfO_x-based memristors by 3D reconstruction,[8] and Liu et al. have prepared a flexible polymer memristor with polyethylenimine mixed with silver salt. The device exhibits a high switching ratio and long holding time.[9] However, the stochastic and unpredictable formation of CF results in variability and significant degradation of device performance and even failure under electrical stimulation. Therefore, it is necessary to control the formation and dynamic process of the switching filament in resistive memory devices.

The resistive properties of memristive devices are influenced by extrinsic effects such as moisture that can diffuse and adsorb to the insulating matrix.[10−13] Yun et al. have reported that devices based on perovskite materials with $FAPbI_3$ degrade rapidly at a relative humidity (RH) of 50%, and the device becomes unstable.[14] Liu et al. have shown that humidity can cause structural damage to electrodes giving rise to random growth and breakage of filaments.[15] Zhou et al. controlled the formation of the H_yMoO_x conductive channel by modulating the intensity of external stimuli to constrain the generation and migration of protons. Protons (H^+) are produced in the MoO_x film by the reaction between holes and absorbed water molecules.[16] In our previous work, a bionic double-layer porous structure was constructed to control the ion transport to improve the memristive performance.[17]

In this work, a regulation strategy combining a porous structure and humidity is designed to fabricate Ag/Porous SiO_x/Si stacks. By changing the etching time and RH, a large on−off ratio of 10^8 and stable resistance states are obtained. The synergistic effects rendered by the porous structure and

Received: May 19, 2023
Accepted: September 12, 2023
Published: September 22, 2023

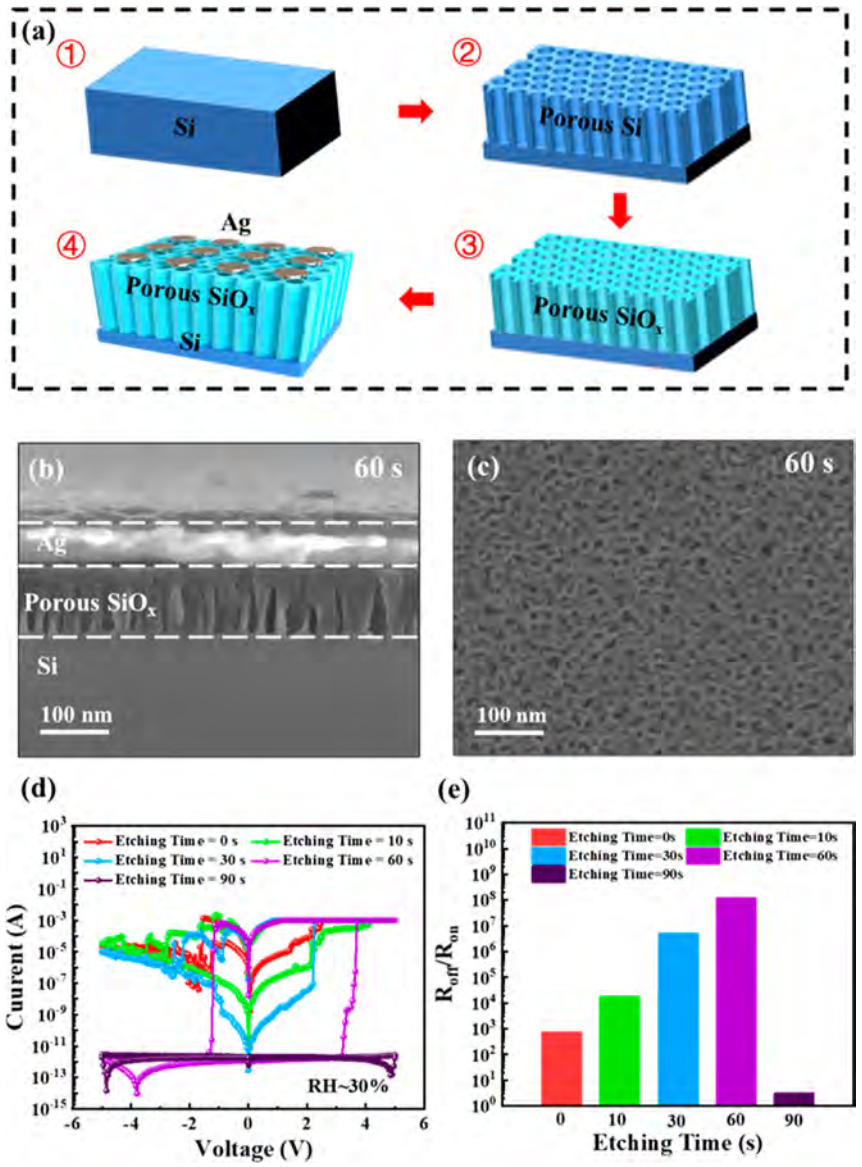

Figure 1. (a) Fabrication process of the memristor with the Ag/Porous SiO_x/Si structure. (b) Cross-sectional SEM image of the stacked resistive switching device in which the porous SiO_x thin film is sandwiched between the tope Ag electrode and bottom Si electrode. (c) Surface of porous SiO_x. (d) *I*–*V* curves of the samples etched for different time durations of 0, 10, 30, 60, and 90 s. (e) On/off ratios of the devices.

environmental humidity provide sites for stable migration of Ag^+ and enable the controlled formation of CF. The feasibility of the device in pattern recognition is studied according to different humidity conditions, and the cognition rates increase from 60.9 to 85.29%. Our findings provide insights into how to optimize the stability of the oxide-based memristors and provide guidance in the development and application to neuromorphic computing (NC).

RESULTS AND DISCUSSION

Porous SiO_x ($PSiO_x$) memristors with different pore sizes and depths are designed and fabricated by a process involving electrochemical anodization and chemical vapor deposition (CVD). The Ag electrode (~80 nm) is deposited on the $PSiO_x$/Si substrate by magnetron sputtering as shown in Figure 1a. The cross-sectional scanning electron microscopy (SEM) images of the Ag/SiO_x/Si stacks and FE-SEM images of $PSiO_x$ of the samples etched for different time durations of 10, 30, 60, and 90 s are depicted in Figures 1b,c and S1, respectively. To determine the properties of the devices, the *I*–*V* characteristics are studied in the voltage sweeping range of 0 V → 5 V → 0 V → −5 V → 0 V for a current compliance of 1 mA and step of 0.05 V, as shown in Figure 1d. The devices exhibit bipolar resistance switching characteristics when the etching time durations are 0, 10, 30, and 60 s, and the maximum current reaches 10^{-3} A in the set progress. When the etching time is 90 s and the scanned voltage range is −5 to 5 V, the device still remains in the HRS. As the etching time increases, the oxide layer thickness increases, as shown in Figure S1a,c,e. A larger threshold voltage is required to form a conductive channel in the set process when the etching time is 90 s, as shown in Figure S2.[18] As the etching time increases from 0 to 60 s, the on/off ratio of the devices increases gradually from 10^3 to 10^8. However, when the etching time is 90 s, the on−off ratio is only 10 at the scanned voltage range of −5 to 5 V, as shown in Figure 1e. By analyzing the *I*–*V* characteristics, the difference in the on−off ratios mainly depends on the change of HRS as shown in Figure 1d. With

https://doi.org/10.1021/acsami.3c07179
ACS Appl. Mater. Interfaces 2023, 15, 46449−46459

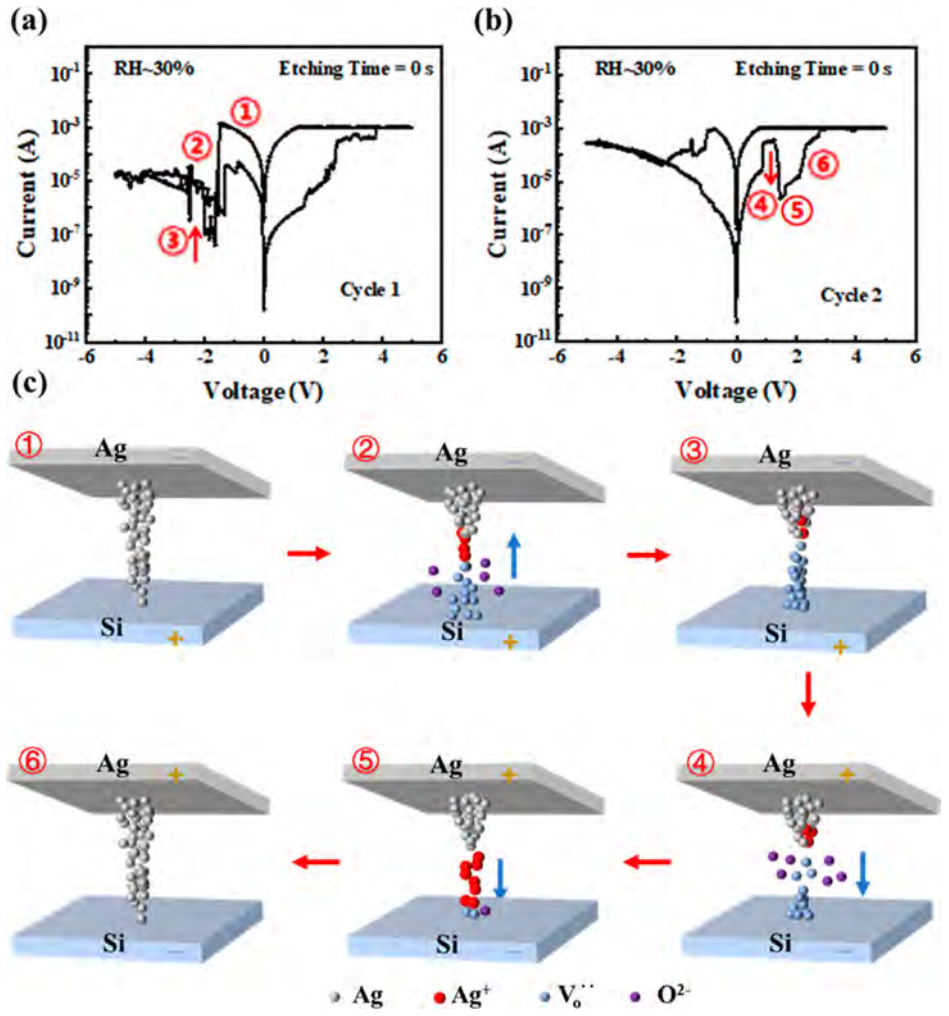

Figure 2. *I*–*V* curves: (a) "negative-set" phenomenon and (b) positive bias. (c) Schematic diagram demonstrating the two-component filament model to explain the origin of the abnormal transition.

increasing etching time, the thickness of the oxide layer (l) increases and R_{HRS} increases[19]

$$R_{device} = R_{Ag} + R_{SiO_x} + R_{Si} \quad (1)$$

and

$$R_{SiO_x} = \rho l/s \quad (2)$$

where R_{Ag} denotes the resistance of the Ag electrode, R_{Si} is the resistance of the Si electrode, ρ represents the resistivity of SiO_x, l is the thickness of SiO_x, and s is the area of the device. In the set process, the charge transport mechanism for different etching time durations of 0, 10, and 30 s follows the Pool–Frankel model shown in Figure S3a and expressed in the following[20−22]

$$I \propto V \exp\left[\frac{q}{kT}(2a\sqrt{V} - \varphi_T)\right] \quad (3)$$

where I is the current, V denotes the applied voltage, q is the electron charge, k is Boltzmann's constant, T is the temperature, φ_T symbolizes the trap depth, and $a = \sqrt{q/4\pi \in_i d}$, where $\in_i$ indicates the insulator permittivity ($\in_i = \in_r \times \in_0$). At the same applied voltage, the relatively large electric field energy enables electrons in the dielectric layer to jump out of defects, and the current changes significantly. For the devices etched for 60 and 90 s, the currents remain almost constant as the voltage is increased from 0 to 3.15 V (Figure 1d) and from 0 to 5.4 V (Figure S2). The corresponding HRS of the device is ~10^{11} Ω, which follows the Hopping conduction mechanism. The ln(I)−V curve derived from the HRS region is displayed in Figure S3b, and the formula of Hopping conduction is shown below[23−25]

$$J = qan\nu \exp\left[\frac{qaE}{kT} - \frac{E_a}{kT}\right] \quad (4)$$

where q is the electronic charge, a is the hopping distance, n is the electron concentration in the conduction band, ν is the frequency of thermal vibration of electrons in the trap states, E_a (activation energy) is the energy from the trap states to the bottom of the conduction band, E is the applied field, k is Boltzmann's constant, and T is the temperature. The linear curves reflect that conduction at the HRS occurs by tunneling of electrons between trap states.

The *I*–*V* characteristics exhibit the "negative-set" phenomenon[26] when the etching time is 0 s, as shown in Figure 2a. Continuous voltage sweeps are applied, and the "positive-reset" phenomenon appears in the second cycle. Subsequently, it can "reset" to HRS and then turn to LRS immediately at a positive voltage, as shown in Figure 2b. This phenomenon happens randomly in different cycles, consequently creating instability

https://doi.org/10.1021/acsami.3c07179
ACS Appl. Mater. Interfaces 2023, 15, 46449−46459

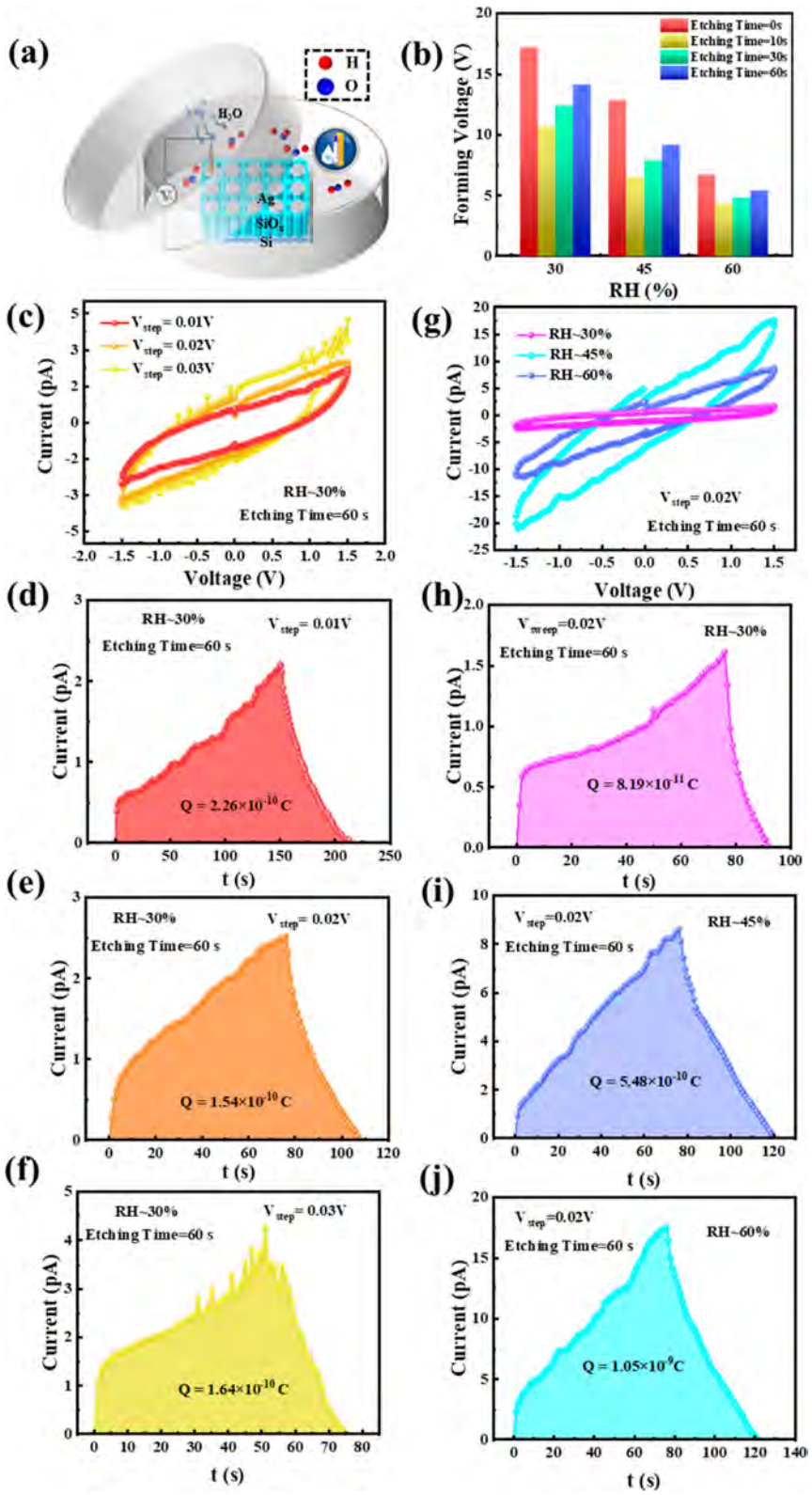

Figure 3. (a) Schematic representation of the atmosphere-controlled electrical measurements (statistical analysis for etching time durations of 0, 10, 30, and 60 s at RH of ~30, ~45, and ~60%). (b) Forming voltages of the devices. (c) *I*−*V* curve of the devices at an RH of ~30% at different sweeping voltage steps: (d) 0.01, (e) 0.02, and (f) 0.03 V. (g) *I*−*V* curve of the devices at the same sweeping rate of 0.02 V for different RHs: (h) ~30, (i) ~45, and (j) ~60%.

of the HRS, as shown in Figure S4 a−c. The phenomenon of the nonporous oxide-based memristors may be attributed to the coexistence of Ag and $V_o^{\bullet\bullet}$,[27] as shown in Figure 2c. After the set process, the device remains in the LRS, and the CF composed of Ag atoms is shown in Figure 2c(①). When a negative bias is applied to the top Ag electrode, the filament is

https://doi.org/10.1021/acsami.3c07179
ACS Appl. Mater. Interfaces 2023, 15, 46449−46459

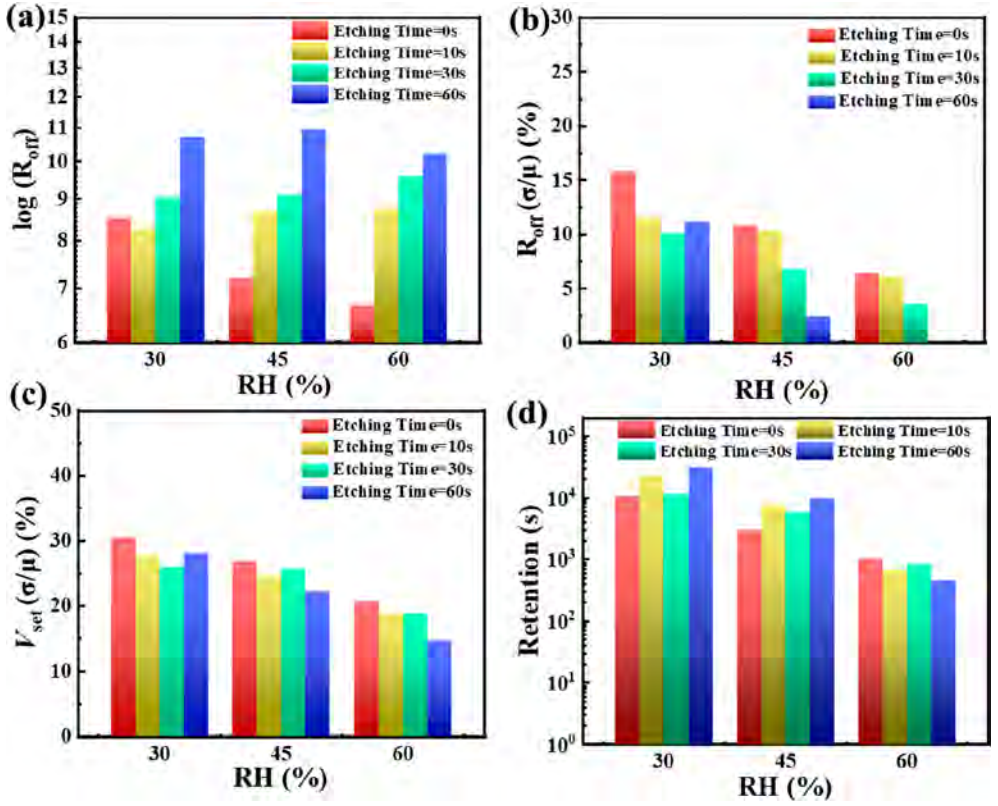

Figure 4. SStatistical analysis of the devices for etching time durations of 0 s, 10 s, 30 s, and 60 s at RH of ∼30%, ∼45%, and ∼60%; (a) log (R_{off}) values of the devices in the endurance test for 128 cycles; (b) Coefficient of variation distribution of log (R_{off}); (c) Coefficient of variation distribution of V_{set}; (d) Retention time of the devices for different etching time durations in the RH range of 30%−60%.

interrupted at a small reset voltage [Figure 2c(②)]. Afterward, when a negative bias is applied continuously, oxygen ions migrate toward the bottom electrode in the broken gaps between the Ag filaments, and the generated $V_o^{\bullet\bullet}$ gradually reconnects the filaments [Figure 2c(③)] to switch the device to the LRS. At a positive voltage, oxygen ions move from the bottom electrode and recombine with $V_o^{\bullet\bullet}$, breaking the filament portion of $V_o^{\bullet\bullet}$ [Figure 2c(④)] and switching the device to the HRS. As positive bias is further applied, the complete Ag filament forms again [Figure 2c(⑤)] and eventually, the device reverts back to the LRS [Figure 2c(⑥)]. In our previous work, porous structures were observed to provide channels for transportation of metal ions.[28] This may give Ag^+ an advantage in competition with $V_o^{\bullet\bullet}$ during migration, thereby avoiding the formation of bipolar filaments.[29] As a result, no negative set phenomenon is observed for the porous devices. To analyze the uniformity of switching in the devices etched for different time durations, the $I-V$ curves of 10 devices acquired by scanning the voltage from −5 to 5 V are analyzed, and Figure S5 reveals similar curves for the same etching time.

To investigate the effects of moisture on the resistive switching behavior of the porous SiO_x films, the memristive behavior of the devices etched for different times and at different humidities is investigated (Figure 3). Figure 3a illustrates the electrical test in a controlled humidity environment. Figure 3b shows the formation voltages of the devices etched for 0, 10, 30, and 60 s in the RH range of ∼30 to ∼60%, and the $I-V$ characteristics of the electroforming process are presented in Figure S6. With increasing RH, the formation voltages decrease significantly due to two rate-limiting processes in the formation of CF, namely, ionization of Ag at the anode interface and migration of Ag^+ in the oxide layer, corresponding to ion production and transport during the formation of conductive channels. In order to investigate the effects of humidity on the former, it is necessary to treat the two-terminal device as an electrochemical cell to study the oxidation-reduction process at the interface.[30,31] Figure 3c,g shows the $I-V$ curves of the device by applying the voltage sweep in the following order 0 → 1.5 → 0 → −1.5 → 0 V, and the $I-V$ curves exhibit analogical cyclic voltammetry behavior of electrochemical reactions. Figure 3c shows the $I-V$ characteristics of the device etched for 60 s at an RH of 30% using voltage sweeping steps of 0.01 0.02, and 0.03 V, respectively. With increasing scanning rates, the peak currents increase, indicative of an inhibited charge transfer controlled reaction at the Ag/porous SiO_x interface. The reduction peak current density can be estimated by the Randles−Sevick equation[32]

$$j_p = 2.69 \times 10^5 \cdot z^{3/2} \cdot c_{ion} \cdot \sqrt{\alpha D \upsilon} \quad (5)$$

where D is the diffusion coefficient, C_{ion} is the ion concentration, z is the number of electrons transferred in the redox reaction, α is the charge transfer coefficient, and υ is the scanning rate. By monitoring the currents during anodic oxidation, the charges involved in the reaction are estimated to be 2.26×10^{-10}, 1.54×10^{-10}, and 1.64×10^{-10} C, respectively, as shown in Figure 3d−f. As the scan rates go up, the time for oxidation reduction is short and therefore, the amount of charges in the reaction decreases and the ion concentration decreases due to the presence of two interfaces,

https://doi.org/10.1021/acsami.3c07179
ACS Appl. Mater. Interfaces 2023, 15, 46449−46459

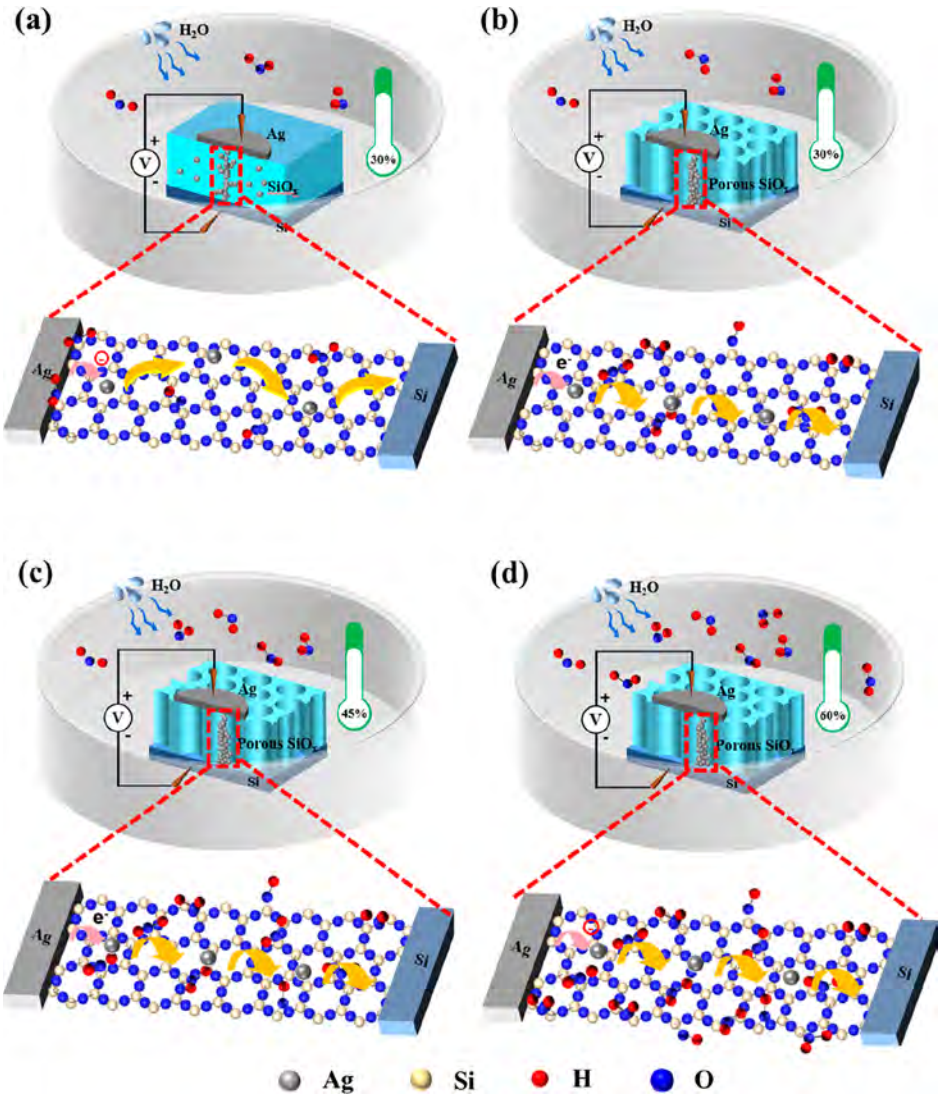

Figure 5. Model explaining the mechanism of the device in the RH range of 30%−60%; (a) Non-porous SiO_x memristor at the indoor RH of ~30%; (b) Porous SiO_x memristor at the indoor RH of ~30%; (c) Porous SiO_x memristor at RH of ~45%. (d) Porous SiOx memristor at RH of ~60%.

the Ag and SiO_x interface and SiO_x and Si interface.[33] The half-cell reaction at the Ag/porous SiO_x interface during anodic oxidation is

$$Ag \rightarrow Ag^+ + e^- \tag{6}$$

The device must be electrically neutral during operation. During the electrochemical reaction, OH^- and water molecules provide the important energy for the electrode reactions through reduction. H_2O molecules provided by the surrounding medium are incorporated into porous SiO_x at room temperature. The half-cell reaction at the cathode interface is

$$\frac{1}{2}H_2O + e^- \rightarrow OH^- + \frac{1}{2}H_2 \tag{7}$$

The effects of humidity on the electrochemical reaction are explored by controlling the voltage sweeping step at 0.02 V in the RH range of ~30 to ~60%, as shown in Figure 3g. With increasing humidity, the number of charges in the reaction increase to 8.19×10^{-11}, 5.48×10^{-10}, and 1.05×10^{-9} C, and the corresponding RH values are 30, 45, and 60%, respectively, as shown in Figure 3h−j. The increase in RH promotes Ag^+ formation at the anode and accelerates the formation of CF, and the forming voltage of the device is reduced. On the other hand, water molecules and hydroxyl species from moisture can adsorb onto the oxide surface to reduce the diffusion barrier of Ag^+ and promote the formation of CF. The reduced diffusion barrier has been shown to be related to the Ag^+ diffusion mechanism. In a humid environment, Ag^+ moves from one water molecule to the other to form Ag−OH complexes that prevent it from interacting with atoms on the SiO_x surface. In the study of Ag^+ diffusion as the rate-limiting step, the formation time τ of the CF is[11]

$$\log \tau = \frac{E_a - \frac{1}{2}e\Delta V}{K_B} \cdot \frac{1}{T} - \log A \tag{8}$$

where E_a is the diffusion barrier for the transition of Ag^+ to adjacent sites, e is the electron charge, ΔV is the effective voltage bias applied between adjacent adsorption sites, K_B is Boltzmann's constant, T is the temperature, and A is a constant. As the RH increases, E_a decreases, log τ decreases, and the forming voltage decreases, as shown in Figure 3b. The

https://doi.org/10.1021/acsami.3c07179
ACS Appl. Mater. Interfaces 2023, 15, 46449−46459

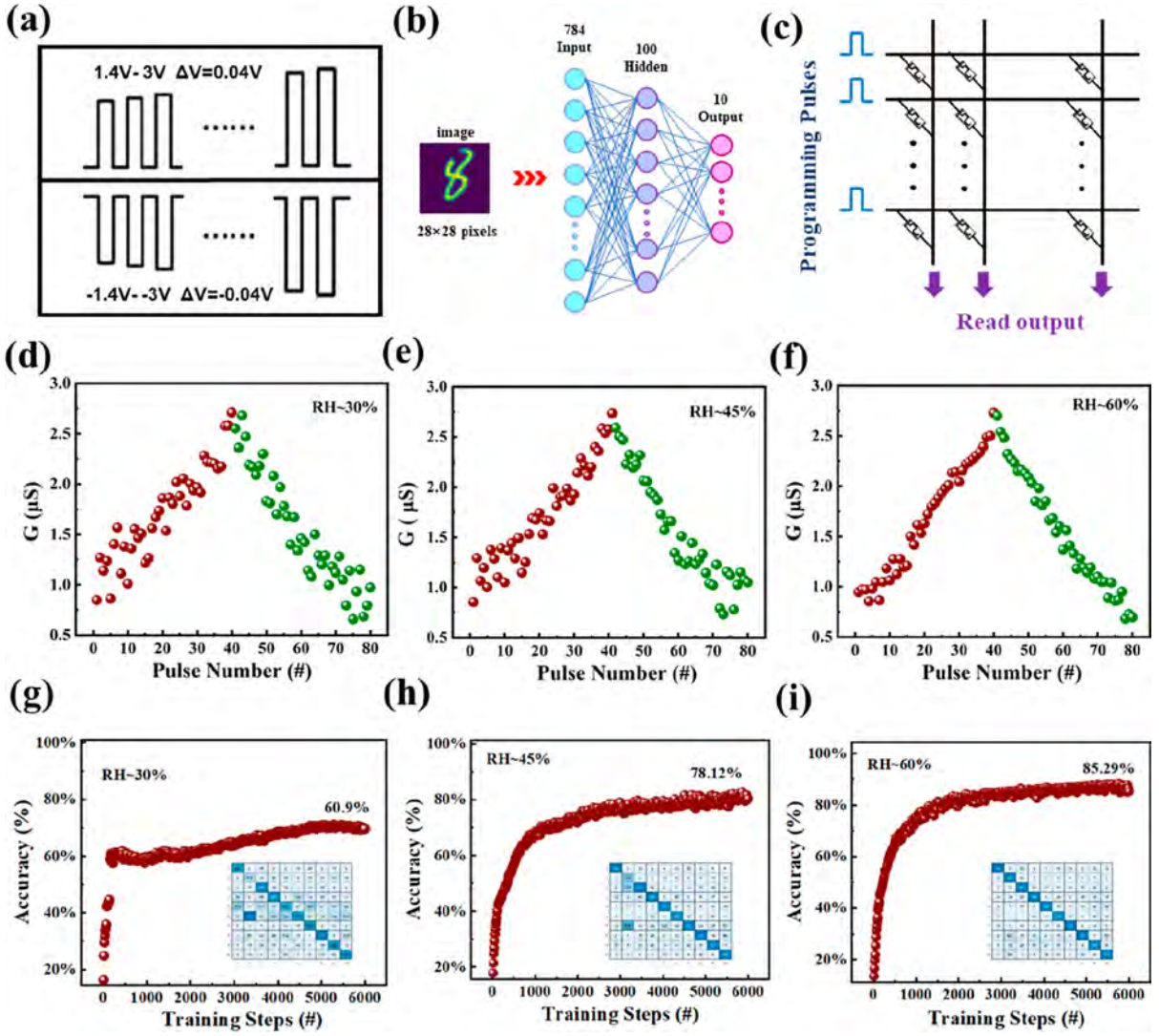

Figure 6. (a) Pulse waveforms under positive and negative voltages; (b) Schematic diagram of the neural network based on image recognition; (c) Schematic of the hardware implementation of the neural network with electrical pulse stimulation implemented in the Ag/porous SiO_x/Si memristors at each intersection; Potentiation and depression by consecutive pulses at (d) RH ~ 30%, (e) RH ~ 45%, (f) RH ~ 60%; Training process of the neural network at (g) RH ~ 30%, (h) RH ~ 45%, (i) RH ~ 60% and demonstrating the confusion matrix of the neural network.

endurance test performed for 128 cycles is shown in Figures S4, S7−S9. In addition, the on/off ratio of devices in the endurance test was 10^3 cycles. The etching time was 60 s and the RH range was 30−60%. The positive/negative pulse amplitude was 5/−7 V and the pulse period was 20 ms, respectively. The pulse width was 10 ms, and the pulse interval was 10 ms, respectively, as shown in Figure S10. The set voltage, reset voltage, HRS, and LRS are statistically analyzed in Figures S11−S14. Figure 4a shows the statistics of the HRS of the samples for different etching times and RHs. The device with the nonporous SiO_x etched for 0 s shows a significant decrease in the HRS with increasing humidity, but no similar trend is observed from the devices etched for 10, 30, and 60 s. We have investigated the competitive mechanism of Ag^+ and $V_o^{\bullet\bullet}$ in the formation of CF in the device.[29] When the humidity is low, the concentration and migration of Ag^+ in the device are suppressed, creating a disadvantage in the competition with $V_o^{\bullet\bullet}$ and resulting in insufficient Ag^+ to form the complete conducting channel. As the forward bias voltage increases, the partial Ag CF enhance the local electric field to promote the generation and migration of $V_o^{\bullet\bullet}$, leading to the formation of a dual-component conducting channel.[34] The formation of CF provides a pathway for electron conduction, and the LRS is almost unaffected by the composition of the CF. When a negative voltage bias is applied, the accumulated $V_o^{\bullet\bullet}$ tends to diffuse, causing the remaining conductive channels to have a larger gap between the electrodes and creating a higher HRS. As the humidity increases gradually, both the concentration and migration ability of Ag^+ increase. It gives Ag^+ an advantage in competition with $V_o^{\bullet\bullet}$, consequently promoting the formation of more complete Ag single-component conductive channels, avoiding the generation and drift of $V_o^{\bullet\bullet}$ under the electric field and reducing the magnitude of HRS. The porous structure can provide a pathway for Ag^+ migration to avoid the occurrence of this phenomenon. Table S1 is the summary of memristive performances for various porous-based memristors such as single porous and array porous. The V_{set}, V_{reset}, endurance cycles, on−off ratio, and retention are summarized. The symbol "×" means that the parameter has not been mentioned in the references. Increasing the humidity may have

https://doi.org/10.1021/acsami.3c07179
ACS Appl. Mater. Interfaces 2023, 15, 46449−46459

a positive impact on the stability of the device. When the RH increases to 75%, the devices etched for different time durations become unstable (Figure S15). Figure 4b,c shows the variations (σ/μ) of the HRS and set voltage, respectively. With increasing RH (~30 to ~60%), the stability of the different devices improves. The stability of devices for an etching time of 0 s is worse than those etched for 10, 30, and 60 s. In a humid environment, water molecules and hydroxyl groups adsorb onto the surface (Figure 5). With regard to the nonporous devices, there is less internal H_2O as shown in Figure 5a, and the migration of Ag^+ in amorphous SiO_x mainly occurs by occupying crystal defects with large randomness. Hence, the nonporous devices at RH of ~30 to ~60% have higher set voltage and HRS dispersion. The porous structure of SiO_x has many hydrogen-bonding sites on the surface of the pores as shown in Figure 5b, which provide binding sites for H_2O molecules. As a result, Ag^+ tends to move on the adsorbed H_2O rather than directly interacting with the SiO_x surface. Ag^+ forms a bond with H_2O, causing H_2O to split into OH^- and H^+ and forming the Ag−OH complex bound to the surface.[35] On the one hand, it reduces the migration energy barrier. On the other hand, the coordination between the porous structure and H_2O forms a "bridge" to stabilize the migration path of Ag^+ and stabilize the growth and fracture of CF. As the RH increases, there are more binding sites to regulate Ag^+ migration (Figure 5b−d), the set voltage and HRS dispersion decrease gradually, and the device stability improves.

To assess the storage characteristics of the devices, the HRS and LRS of the devices etched for different time durations are subjected to retention tests at different RH values (Figure S16). The retention of the HRS can exceed 10^4 s, and it is almost unaffected by the increase in RH. However, the retention time of the LRS decreases significantly with increasing RH, as shown in Figure 4d. When the RH goes up to 60%, the retention time is only a few hundred seconds. In order to investigate the physical mechanism behind the decrease in the LRS retention time with increasing RH, a model based on classical nucleation theory is adopted to describe the dissolution process of CF from a continuous state to dispersed small clusters after the voltage is turned off. When an external electric field is applied, the nucleation barrier energy decreases, making it easier for Ag^+ to aggregate and form a CF. After turning off the voltage, the nucleation barrier energy increases. Owing to the nonvolatile nature of the device, a larger size is required to maintain the thermodynamic stability of the CF. For better interpretation, it is assumed that the easily broken part at the tip of the formed CF has an approximate cylindrical shape with a length of L (Figure S17a). In this case, ΔG represents the change in the Gibbs free energy between the CF state at the tip and the dispersed Ag small cluster state. ΔG is calculated as follows[36]

$$\Delta G = -\pi r^2 L|G_v| + \pi r^2(\gamma_T + \gamma_B) + 2\pi r L\gamma_D \quad (9)$$

where r and L are the radius and length of the cylindrical CF tip, respectively, $|G_v|$ is the Gibbs free energy difference per unit volume, and γ_T, γ_B, and γ_D are the surface energy per unit area of this part of CF in contact with the upper and lower surfaces and the dielectric layer, respectively. Accordingly, the critical size r^* can be obtained by solving for $\Delta G/\Delta r = 0$

$$r^* = \frac{L\gamma_D}{L|G_V| - \gamma_T - \gamma_B} \quad (10)$$

If the radius of the CF tip is smaller than the critical size r^*, then the CF tends to decompose into silver clusters. If the radius of the CF tip is larger than the critical size r^*, then the CF is still thermodynamically stable even in the absence of electrical stimulation (see Figure S17a). As the RH increases, many H_2O molecules adsorb onto the porous silicon oxide walls, and the Ag dangling bonds on the surface of the CF are activated by H_2O to cause γ_D to increase. As a result, the critical size r^* of the CF fracture increases (see Figure S17b). Moreover, the outer Ag atoms of the CF are easily affected by H_2O and diffuse, resulting in a gradual decrease in the actual size of the CF (see Figure S17c−e) and as RH increases, this effect becomes more pronounced. When the actual radius of the CF tip $r < r^*$, it will break and therefore, as humidity increases, the retention time of the device tends to decrease.

To explore the application potential of the device in NC in different humidity environments, a handwritten artificial neural network (ANN) to learn digits from the modified National Institute of Standards and Technology data set using the backpropagation neural network[37] simulator is developed (Figure 6). The release and suppression of the internal ions in the device are associated with enhancement and suppression of the synaptic behavior. The conductance of the device corresponds to the synaptic weight, and behavior similar to the nonlinear transmission characteristics of biological synapses is simulated. Figure 6a shows the positive applied voltage pulses from 1.4 to 3 V in steps of 0.04 V with a 50% duty cycle as well as negative pulses from −1.4 to −3 V in steps of −0.04 V with a 50% duty cycle. The simulator is capable of recognizing image versions utilizing 784 input neurons, 100 hidden neurons, and 10 output neurons, as shown in Figure 6b. The outputs of the first layer are the input signals of synaptic circuits of the second layer, while the last layer makes decisions based on the features extracted from the information. The hardware of the ANN consists of a crossbar structure where the Ag/porous SiO_x/Si devices are located at each cross point, as shown in Figure 6c. Figure 6d−f shows the testing pulses in the RH range of 30−60%. The device conductivity increases or decreases continuously, representing enhancement or suppression of the memristive synapses. This gradual change in conductivity may be caused by the accumulation and diffusion of atoms in the local filamentary conduction mechanism. The conductivity fluctuation is significant at the RH of 30% and as the RH increases, the enhanced/inhibitory behavior stabilizes. Ions in the charged pores may play an important role in the multi-ion Coulomb blockade. Conductance oscillations may originate from multi-ion interactions at the pore entrance, especially electrostatic repulsion between the external ions and bound ions inside the pore. When Ag^+ is produced from the electrode and moves to the pores, electrostatic potential barriers are formed on both sides of the pore due to the presence of multiple Ag^+ that have already entered the pore. This interaction causes Coulombic repulsion toward Ag^+ outside the pore. Due to the promotion of the half-cell reaction at the interface of the two electrodes inside the device and hydroxide ions in the humid environment, many negatively charged OH^- absorb to the pore walls. These OH^- ions reduce the electrostatic potential barrier produced by the accumulation of positively charged Ag^+ both inside and outside the pore. With increasing RH, the increase of OH^-

https://doi.org/10.1021/acsami.3c07179
ACS Appl. Mater. Interfaces 2023, 15, 46449−46459

ions reduces the Coulombic repulsion, and the conductivity oscillation and conductivity fluctuation decrease gradually. Figure 6g–i shows the training process of the network after 6000 training rounds as the RH increases gradually from 30 to 60%. The accuracy of the ideal software for the training set increases from 60.9 to 85.29%. The lower right corner in Figure 6g–i shows the confusion matrix of the network, which compares the calculated results with the labels of the test set and comprehensively demonstrates the classification performance of the network. The values of the diagonal of the confusion matrix are the numbers of correct classifications for each digit, and as the humidity increases, the accuracy is higher.

CONCLUSIONS

Humidity is used to control the Ag^+ migration step-by-step in the porous SiO_x memristor. The resistive switching characteristics vary according to the dissolution and migration of ions (Ag^+), and the device has stable memristive properties and large on–off ratios. Moisture is found to regulate the conductance fluctuations generated in the enhancement/suppression of synaptic behavior simulation. Our findings provide important insights for the development of high-performance memristors under the influence of humidity.

EXPERIMENTAL SECTION

Preparation of Porous SiO_x. The highly doped Si wafer (ρ < 0.0015 Ω·m and $d = 375 \pm 25$ μm) underwent electrochemical anodic oxidation in a solution containing 10 vol % HF (≥40%, Sinopharm Chemical Reagent Co., Ltd.) using the constant current mode of 60 mA/cm^2 for 60 s at room temperature. Porous SiO_x (~100 nm thick, Ø ~ 10 nm) was prepared on the porous p-type (100) Si substrate by CVD at 900 °C for 1 h under an oxygen flow rate of 60 sccm as shown in Figure 1a.

Preparation of the Ag/Porous SiO_x/Si Device. The Ag layer (~80 nm) was prepared on the SiO_x/Si substrate by magnetron sputtering. The size of the device was about 0.785 mm^2.

Electrical Characterization. Electrical characterization of the atmospheric control was carried out in a closed environment. The humidification equipment and humidity controller were adopted, and the humidification equipment was filled with deionized water. The RH in the room was measured with a simulated humidity sensor. The electrical measurements were performed under stable ambient conditions using a Keithley SCS4200 and AFG31000 series arbitrary function generator. During the tests, Si was the negative electrode, and Ag was the positive electrode. A compliance current of 1 mA was applied to prevent complete breakdown of the device, and all the electrical measurements were carried out at room temperature.

ASSOCIATED CONTENT

Supporting Information

The Supporting Information is available free of charge at https://pubs.acs.org/doi/10.1021/acsami.3c07179.

SEM images of the devices fabricated using different etching times; I–V curve of the device with an etching time of 90 s; conduction mechanism of the Ag/SiO_x/Si of HRS with etching time durations of 0, 10, 30, 60, and 90 s; endurance test of the device with an etching time of 0 s in the RH range of 30–60%; uniformity of the devices for different etching times; formation voltages of the devices for different etching times; endurance test of the device using an etching time of 10 s in the RH range of 30–60%; endurance test of the device using an etching time of 30 s in the RH range of 30–60%; endurance test of the device using an etching time of 60 s in the RH range of 30–60%; endurance test by pulse mode of the device using an etching time of 60 s in the RH range of 30–60%; statistics of the voltages and resistance states of the devices using an etching time of 0 s in the RH range of 30–60%; statistics of the voltages and resistance states of the devices using an etching time of 10 s in the RH range of 30–60%; statistics of the voltages and resistance states of the devices using an etching time of 30 s in the RH range of 30–60%; statistics of the voltages and resistance states of the devices using an etching time of 60 s in the RH range of 30–60%; I–V curves of the devices using different etching time durations at an RH of 75%; retention characteristics of the devices using different etching time durations in the RH range of 30–60%; comparison of the performance with other similar devices; and physical mechanism of the devices with decreasing retention time with increasing RH (PDF)

AUTHOR INFORMATION

Corresponding Author

Anping Huang – *School of Physics, Beihang University, Beijing 100191, China;* orcid.org/0000-0002-1365-3575; Email: aphuang@buaa.edu.cn

Authors

Haoze Li – *School of Physics, Beihang University, Beijing 100191, China*

Qin Gao – *School of Physics and School of Chemistry, Beihang University, Beijing 100191, China;* orcid.org/0000-0002-0573-9774

Juan Gao – *School of Physics, Beihang University, Beijing 100191, China*

Jiangshun Huang – *School of Physics, Beihang University, Beijing 100191, China*

Xueli Geng – *School of Physics, Beihang University, Beijing 100191, China*

Guoxing Wang – *School of Physics, Beihang University, Beijing 100191, China*

Bo Liang – *School of Physics, Beihang University, Beijing 100191, China*

Xinghe Li – *School of Physics, Beihang University, Beijing 100191, China*

Mei Wang – *School of Physics, Beihang University, Beijing 100191, China*

Zhisong Xiao – *School of Physics, Beihang University, Beijing 100191, China;* orcid.org/0000-0001-7309-9900

Paul K. Chu – *Department of Physics, Department of Materials Science and Engineering, and Department of Biomedical Engineering, City University of Hong Kong, Kowloon, Hong Kong 999077, China;* orcid.org/0000-0002-5581-4883

Complete contact information is available at: https://pubs.acs.org/10.1021/acsami.3c07179

Author Contributions

H.L. and Q.G. contributed equally to this work. H.L. and Q.G. designed and performed the experiments and wrote the manuscript, and Q.G. corrected the manuscript. J.G., J.H., X.G., G.W., B.L., X.L., M.W., Z.X., P.K.C, A.H. assisted in data analysis. P.K.C. corrected the manuscript. All authors

https://doi.org/10.1021/acsami.3c07179
ACS Appl. Mater. Interfaces 2023, 15, 46449–46459

interpreted the data and wrote the manuscript. A.H. planned and supervised all phases of the project and corrected the manuscript.

Notes

The authors declare no competing financial interest.

■ ACKNOWLEDGMENTS

This research was supported by the National Natural Science Foundation of China (grant nos. 51872010 and 61975005), Foundation of Beijing Academy of Quantum Information Sciences (grant no. Y18G28), and City University of Hong Kong Donation Research Grant (DON-RMG no. 9229021).

■ REFERENCES

(1) Gao, B.; Zhou, Y.; Zhang, Q.; Zhang, S.; Yao, P.; Xi, Y.; Liu, Q.; Zhao, M.; Zhang, W.; Liu, Z.; Li, X.; Tang, J.; Qian, H.; Wu, H. Memristor-based analogue computing for brain-inspired sound localization with in situ training. *Nat. Commun.* **2022**, *13*, 2026.

(2) Rao, M.; Tang, H.; Wu, J.; Song, W.; Zhang, M.; Yin, W.; Zhuo, Y.; Kiani, F.; Chen, B.; Jiang, X.; Liu, H.; Chen, H. Y.; Midya, R.; Ye, F.; Jiang, H.; Wang, Z.; Wu, M.; Hu, M.; Wang, H.; Xia, Q.; Ge, N.; Li, J.; Yang, J. J. Thousands of conductance levels in memristors integrated on CMOS. *Nature* **2023**, *615*, 823−829.

(3) Kim, Y. S.; An, J.; Jeon, J. B.; Son, M. W.; Son, S.; Park, W.; Lee, Y.; Park, J.; Kim, G. Y.; Kim, G.; Song, H.; Kim, K. M. Ternary Logic with Stateful Neural Networks Using a Bilayered TaO_x-Based Memristor Exhibiting Ternary States. *Adv. Sci.* **2022**, *9*, 2104107.

(4) Teng, C.; Yu, Q.; Sun, Y.; Ding, B.; Chen, W.; Zhang, Z.; Liu, B.; Cheng, H.-M. Homologous gradient heterostructure-based artificial synapses for neuromorphic computation. *InfoMat* **2023**, *5*, No. e12351.

(5) Zhang, Y.; Mao, G.-Q.; Zhao, X.; Li, Y.; Zhang, M.; Wu, Z.; Wu, W.; Sun, H.; Guo, Y.; Wang, L.; Zhang, X.; Liu, Q.; Lv, H.; Xue, K.-H.; Xu, G.; Miao, X.; Long, S.; Liu, M. Evolution of the conductive filament system in HfO_2-based memristors observed by direct atomic-scale imaging. *Nat. Commun.* **2021**, *12*, 7232.

(6) Song, Y. G.; Suh, J. M.; Park, J. Y.; Kim, J. E.; Chun, S. Y.; Kwon, J. U.; Lee, H.; Jang, H. W.; Kim, S.; Kang, C. Y.; Yoon, J. H. Artificial Adaptive and Maladaptive Sensory Receptors Based on a Surface-Dominated Diffusive Memristor. *Adv. Sci.* **2022**, *9*, 2103484.

(7) Cha, J. H.; Yang, S. Y.; Oh, J.; Choi, S.; Park, S.; Jang, B. C.; Ahn, W.; Choi, S. Y. Conductive-bridging random-access memories for emerging neuromorphic computing. *Nanoscale* **2020**, *12*, 14339−14368.

(8) Wei, T.; Lu, Y.; Zhang, F.; Tang, J.; Gao, B.; Yu, P.; Qian, H.; Wu, H. Three-Dimensional Reconstruction of Conductive Filaments in HfO_x-Based Memristor. *Adv. Mater.* **2023**, *35*, 2209925.

(9) Zhang, X.; Wu, C.; Lv, Y.; Zhang, Y.; Liu, W. High-Performance Flexible Polymer Memristor Based on Stable Filamentary Switching. *Nano Lett.* **2022**, *22*, 7246−7253.

(10) Aiba, A.; Kaneko, S.; Tsuruoka, T.; Terabe, K.; Kiguchi, M.; Nishino, T. Effects of water adsorption on conductive filaments of a Ta_2O_5 atomic switch investigated by nondestructive electrical measurements. *Appl. Phys. Lett.* **2020**, *117*, 233104.

(11) Mikami, M.; Tanahashi, N.; Tsuruoka, T.; Hasegawa, T. Changes in the temperature dependence of $Ag/Ta_2O_5/Pt$ gapless-type atomic switches caused by desorption/adsorption of water molecules from/into the Ta_2O_5 matrix. *J. Appl. Phys.* **2021**, *60*, Sccf05.

(12) Tao, Y.; Wang, Z.; Xu, H.; Ding, W.; Zhao, X.; Lin, Y.; Liu, Y. Moisture-powered memristor with interfacial oxygen migration for power-free reading of multiple memory states. *Nano Energy* **2020**, *71*, 104628.

(13) Zhang, X.; Zhao, X.; Shan, X.; Tian, Q.; Wang, Z.; Lin, Y.; Xu, H.; Liu, Y. Humidity Effect on Resistive Switching Characteristics of the $CH_3NH_3PbI_3$ Memristor. *ACS Appl. Mater. Interfaces* **2021**, *13*, 28555−28563.

(14) Yun, J. S.; Kim, J.; Young, T.; Patterson, R. J.; Kim, D.; Seidel, J.; Lim, S.; Green, M. A.; Huang, S.; Ho-Baillie, A. Humidity-Induced Degradation via Grain Boundaries of $HC(NH_2)_2PbI_3$ Planar Perovskite Solar Cells. *Adv. Funct. Mater.* **2018**, *28*, 1705363.

(15) Liu, K.; Qin, L.; Zhang, X.; Zhu, J.; Sun, X.; Yang, K.; Cai, Y.; Yang, Y.; Huang, R. Interfacial redox processes in memristive devices based on valence change and electrochemical metallization. *Faraday Discuss.* **2019**, *213*, 41−52.

(16) Zhou, F.; Zhou, Z.; Chen, J.; Choy, T. H.; Wang, J.; Zhang, N.; Lin, Z.; Yu, S.; Kang, J.; Wong, H. S. P.; Chai, Y. Optoelectronic resistive random access memory for neuromorphic vision sensors. *Nat. Nanotechnol.* **2019**, *14*, 776−782.

(17) Gao, Q.; Huang, A.; Zhang, J.; Ji, Y.; Zhang, J.; Chen, X.; Geng, X.; Hu, Q.; Wang, M.; Xiao, Z.; Chu, P. K. Artificial synapses with a sponge-like double-layer porous oxide memristor. *NPG Asia Mater.* **2021**, *13*, 3.

(18) Ambrosi, E.; Bricalli, A.; Laudato, M.; Ielmini, D. Impact of oxide and electrode materials on the switching characteristics of oxide ReRAM devices. *Faraday Discuss.* **2019**, *213*, 87−98.

(19) Valov, I.; Linn, E.; Tappertzhofen, S.; Schmelzer, S.; van den Hurk, J.; Lentz, F.; Waser, R. Nanobatteries in redox-based resistive switches require extension of memristor theory. *Nat. Commun.* **2013**, *4*, 1771.

(20) Song, Y.; Wang, X.; Wu, Q.; Wang, C.; Du, S.; Zhang, L.; Miao, X. High switching uniformity in HfO_x-based memristors by adding polydopamine-derived Ag nanoparticles on the electrode. *Appl. Phys. Lett.* **2021**, *118*, 223501.

(21) Chiu, F. C. A Review on Conduction Mechanisms in Dielectric Films. *Adv. Mater. Sci. Eng.* **2014**, *2014*, 1−18.

(22) Park, J.; Kim, S. Improving endurance and reliability by optimizing the alternating voltage in Pt/ZnO/TiN RRAM. *Results Phys.* **2022**, *39*, 105731.

(23) Ben Taher, Y.; Oueslati, A.; Maaloul, N. K.; Khirouni, K.; Gargouri, M. Conductivity study and correlated barrier hopping (CBH) conduction mechanism in diphosphate compound. *Appl. Phys. A: Mater. Sci. Process.* **2015**, *120*, 1537−1543.

(24) Mondal, T.; Das, S.; Sinha, T. P.; Sarun, P. M. Dielectric relaxation and study of electrical conduction mechanism in $BaZr_{0.1}Ti_{0.9}O_3$ ceramics by correlated barrier hopping model. *Mater. Sci. Polym.* **2018**, *36*, 112−122.

(25) Cuhadar, C.; Kim, S. G.; Yang, J. M.; Seo, J. Y.; Lee, D.; Park, N. G. All-Inorganic Bismuth Halide Perovskite-Like Materials $A_3Bi_2I_9$ and $A_3Bi_{1.8}Na_{0.2}I_{8.6}$ (A = Rb and Cs) for Low-Voltage Switching Resistive Memory. *ACS Appl. Mater. Interfaces* **2018**, *10*, 29741−29749.

(26) Li, P.; Wang, D.; Zhang, Z.; Guo, Y.; Jiang, L.; Xu, C. Room-Temperature, Solution-Processed SiO_x via Photochemistry Approach for Highly Flexible Resistive Switching Memory. *ACS Appl. Mater. Interfaces* **2020**, *12*, 56186−56194.

(27) Li, P.; Zhang, Y.; Guo, Y.; Jiang, L.; Zhang, Z.; Xu, C. Resistance Switching Behavior of a Perhydropolysilazane-Derived SiO_x-Based Memristor. *J. Phys. Chem. Lett.* **2021**, *12*, 10728−10734.

(28) Gao, Q.; Huang, J.; Gao, J.; Geng, X.; Ji, Y.; Li, H.; Wang, G.; Liang, B.; Wang, M.; Xiao, Z.; Zhu, Y.; Chu, P. K.; Huang, A. Tunable plasticity in functionalized honeycomb synaptic memristor for neurocomputing. *Mater. Today Phys.* **2023**, *30*, 100947.

(29) Hu, Q.; Fan, Z.; Huang, A.; Zhang, X.; Zhao, R.; Gao, Q.; Ji, Y.; Dou, W.; Wang, M.; Shi, H.; Xiao, Z.; Jiang, X.; Chu, P. K. Competitive conductive mechanism of interstitial Ag and oxygen vacancies in $Ag/Ta_2O_5/Pt$ stack. *J. Appl. Phys.* **2019**, *126*, 065104.

(30) Tsuruoka, T.; Valov, I.; Mannequin, C.; Hasegawa, T.; Waser, R.; Aono, M. Humidity effects on the redox reactions and ionic transport in a $Cu/Ta_2O_5/Pt$ atomic switch structure. *J. Appl. Phys.* **2016**, *55*, 06gj09.

(31) Lübben, M.; Valov, I. Active Electrode Redox Reactions and Device Behavior in ECM Type Resistive Switching Memories. *Adv. Electron. Mater.* **2019**, *5*, 1800933.

https://doi.org/10.1021/acsami.3c07179
ACS Appl. Mater. Interfaces 2023, 15, 46449−46459

(32) Tappertzhofen, S.; Mundelein, H.; Valov, I.; Waser, R. Nanoionic transport and electrochemical reactions in resistively switching silicon dioxide. *Nanoscale* **2012**, *4*, 3040−3043.
(33) Tappertzhofen, S.; Valov, I.; Tsuruoka, T.; Hasegawa, T.; Waser, R.; Aono, M. Generic relevance of counter charges for cation-based nanoscale resistive switching memories. *ACS Nano* **2013**, *7*, 6396−6402.
(34) Chang, C. F.; Chen, J. Y.; Huang, C. W.; Chiu, C. H.; Lin, T. Y.; Yeh, P. H.; Wu, W. W. Direct Observation of Dual-Filament Switching Behaviors in Ta_2O_5-Based Memristors. *Small* **2017**, *13*, 1603116.
(35) Milano, G.; Raffone, F.; Luebben, M.; Boarino, L.; Cicero, G.; Valov, I.; Ricciardi, C. Water-Mediated Ionic Migration in Memristive Nanowires with a Tunable Resistive Switching Mechanism. *ACS Appl. Mater. Interfaces* **2020**, *12*, 48773−48780.
(36) Ding, X.; Huang, P.; Zhao, Y.; Feng, Y.; Liu, L. Understanding of the Volatile and Nonvolatile Switching in Ag-Based Memristors. *IEEE Trans. Electron Devices* **2022**, *69*, 1034−1040.
(37) Xiao, B.; Watanabe, S. Moisture effect on the diffusion of Cu ions in Cu/Ta_2O_5/Pt and Cu/SiO_2/Pt resistance switches: a first-principles study. *Sci. Technol. Adv. Mater.* **2019**, *20*, 580−588.

https://doi.org/10.1021/acsami.3c07179
ACS Appl. Mater. Interfaces 2023, 15, 46449−46459

Supporting Information

Controllability of the Conductive Filament in Porous SiOx Memristors by Humidity-Mediated Silver Ion Migration

Haoze Li,[1] *Qin Gao*,[2] *Juan Gao*,[1] *Jiangshun Huang*,[1] *Xueli Geng*,[1] *Guoxing Wang*,[1] *Bo Liang*,[1] *Xinghe Li*,[1] *Mei Wang*,[1] *Zhisong Xiao*,[1] *Paul K. Chu*,[3] *Anping Huang*[1*]

[1] School of Physics, Beihang University, Beijing 100191, China

[2] School of Physics and School of Chemistry, Beihang University, Beijing 100191, China

[3] Department of Physics, Department of Materials Science and Engineering, and Department of Biomedical Engineering, City University of Hong Kong, Tat Chee Avenue, Kowloon, Hong Kong 999077, China

**** Corresponding Authors***

Anping Huang − Email: aphuang@buaa.edu.cn (Dr. A. P. Huang)

1. SEM images of devices with different etching times

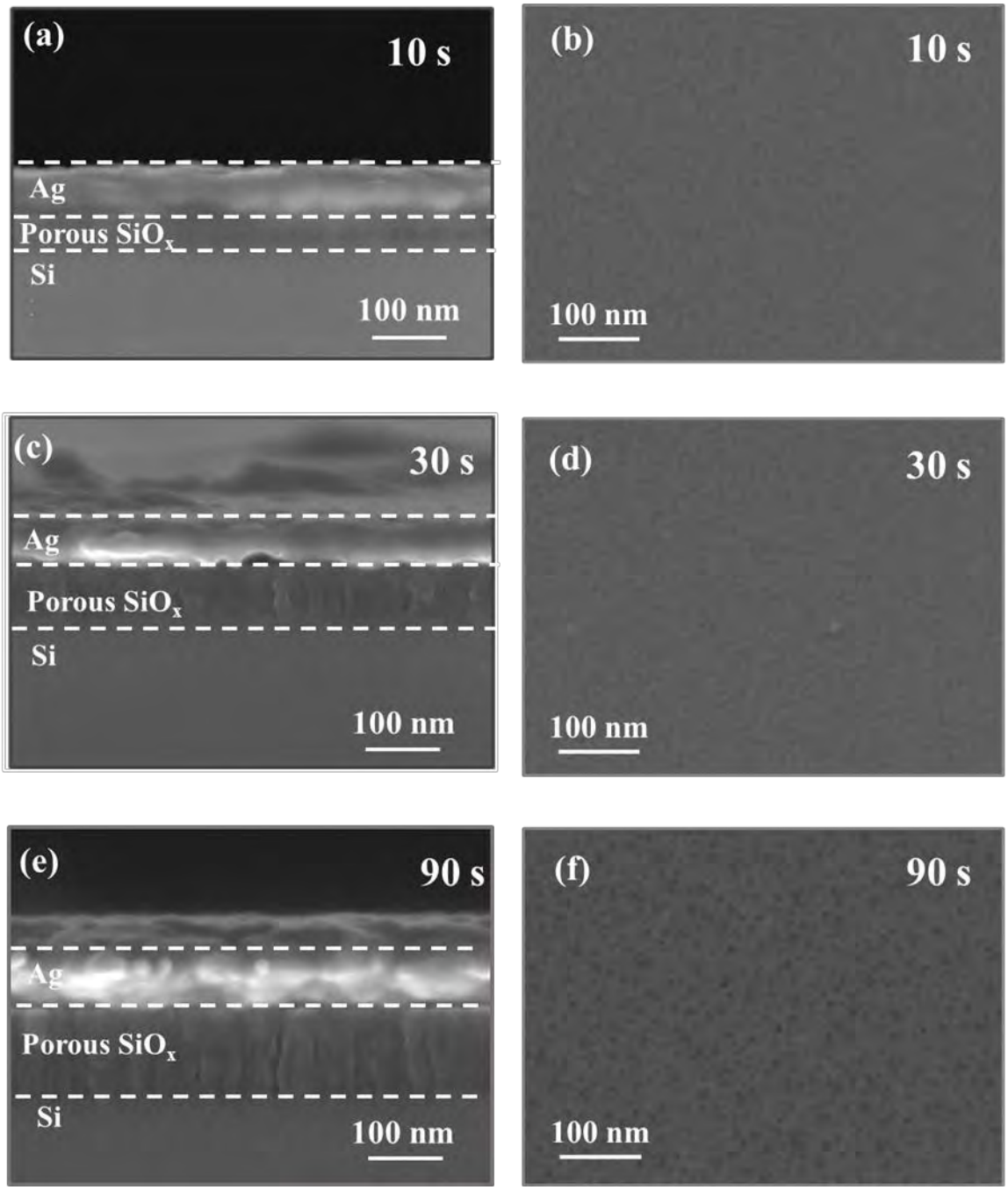

Figure S1. SEM images of the cross-sections of Ag/Porous SiO_x/Si devices etched for (a) 10 s, (b) 30 s, and (c) 90 s. Surface of Porous SiO_x etched for (d) 10 s, (e) 30 s, and (f) 90 s.

2. *I-V* curve of the device with the etching time of 90 s

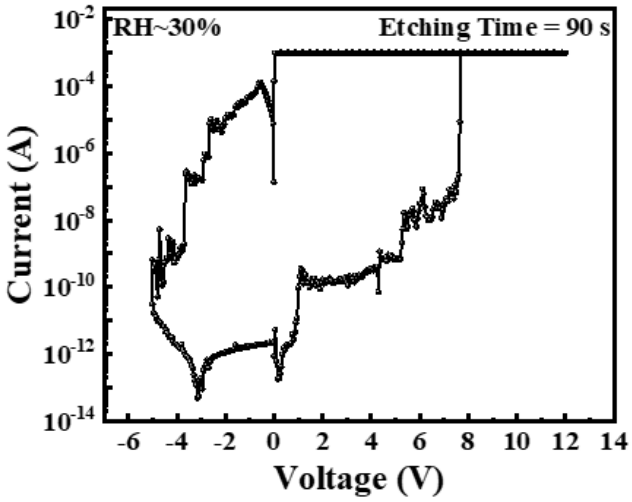

Figure S2. *I-V* curve of the device with the eching of 90 s and the RH is about 30% (indoor humidity). The SET voltage of the device with the etching time is 90 s is higher than 5 V.

3. Conduction mechanism analysis of Ag/SiO_x/Si of HRS with etching time of 0 s, 10 s, 30 s, 60 s and 90 s

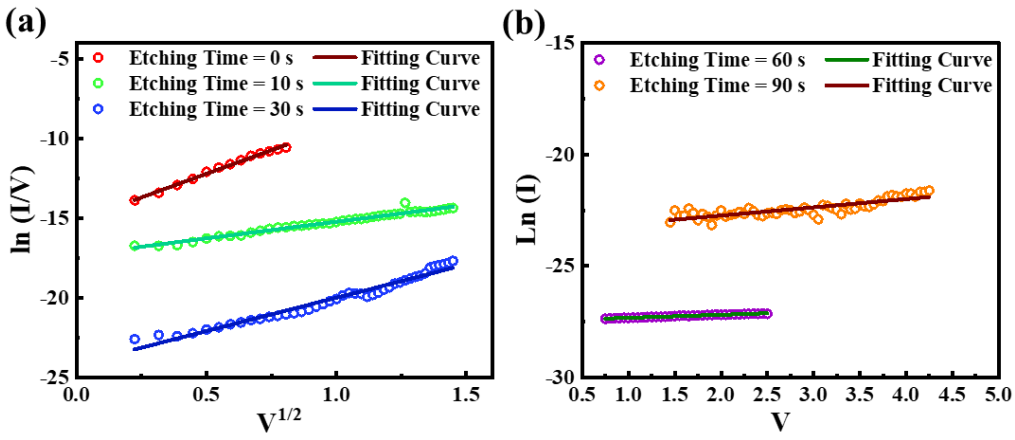

Figure S3. Fittings curve for HRS of Ag/SiO_x/Si devices with the etching time of (a) 0 s, 10 s, 30 s, (b) 60 s and 90 s.[1]

4. Endurance test of the device with the etching time is 0 s at the range of RH 30%-60%

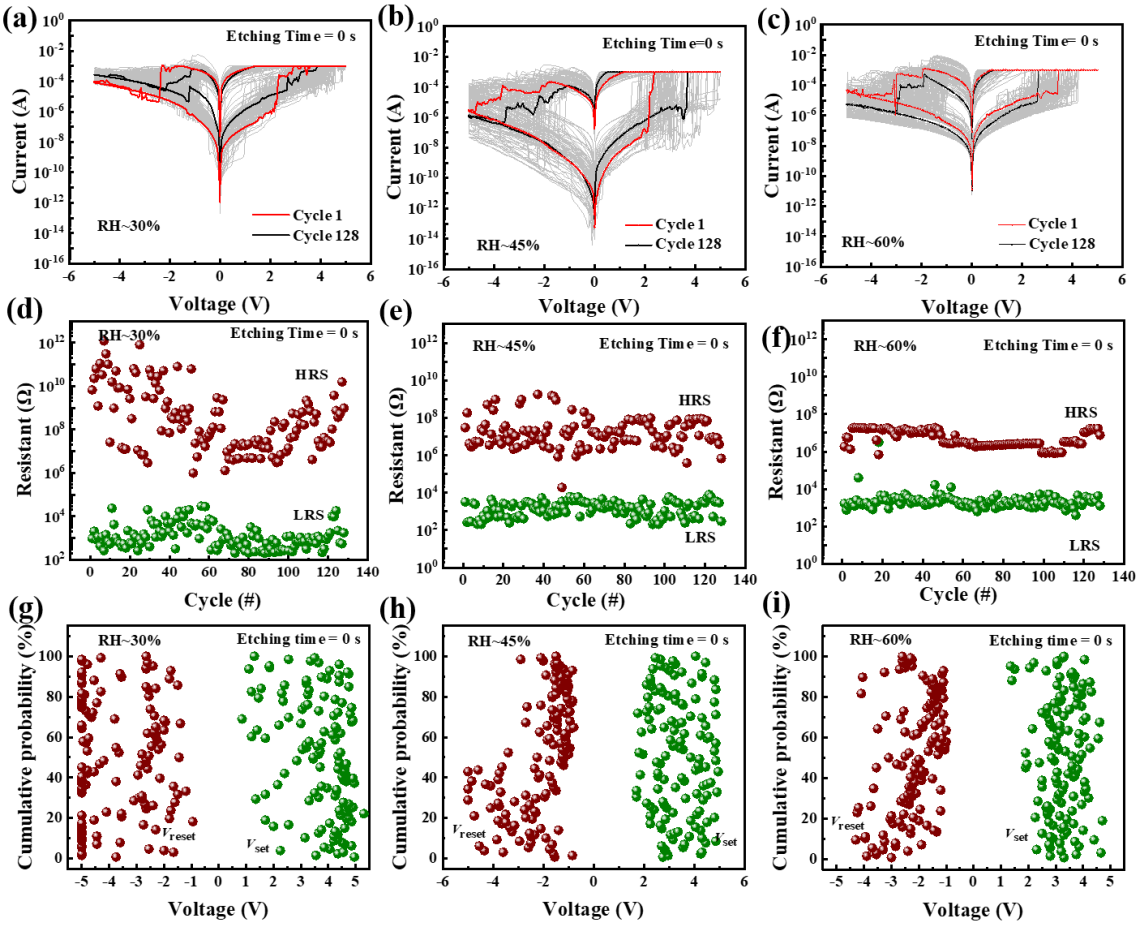

Figure S4. (a)-(c) *I-V* curves of SiO_x memristors with different RH range; (d)-(f) Endurance of SiO_x memristors with different RH range; (g)-(i) cumulative probability of SET voltage and RESET voltage of SiO_x memristors with different RH range.

5. Uniformity of devices at different etching times

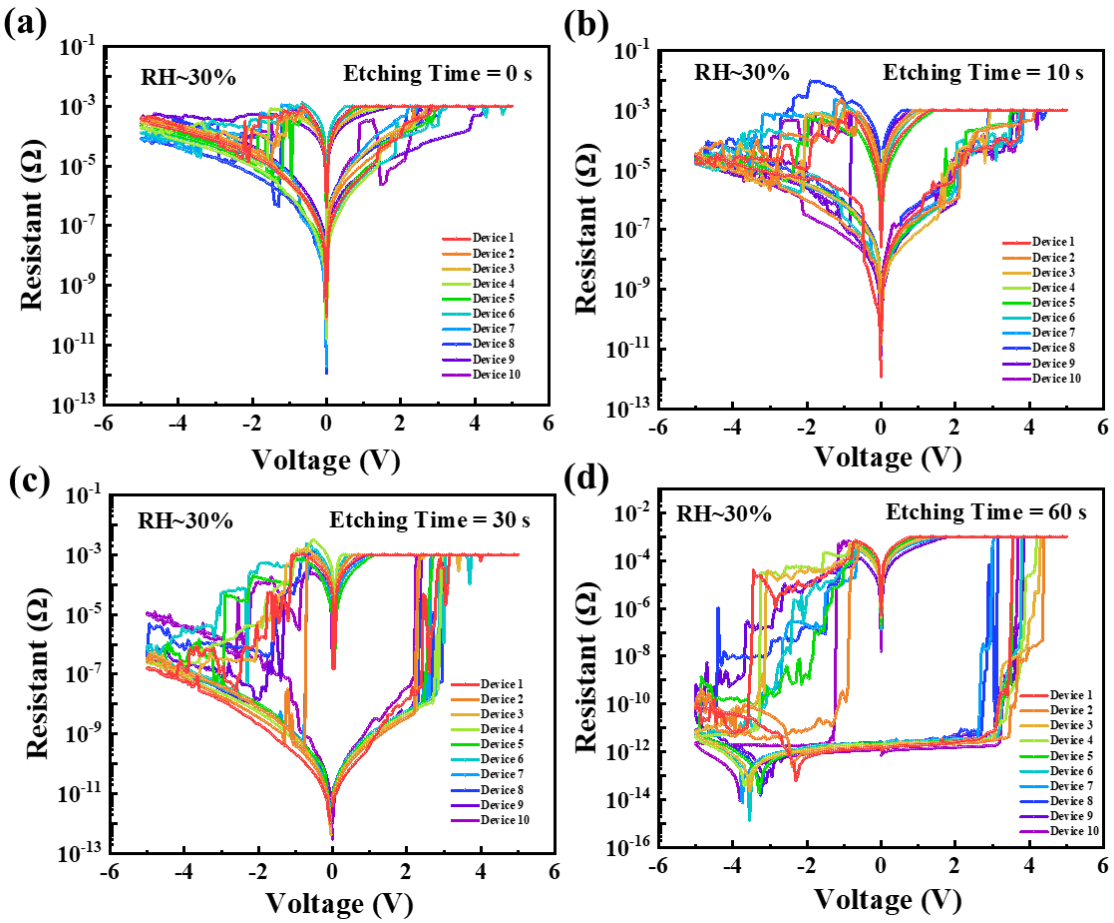

Figure S5. Reproducibility of the *I-V* curve among 10 devices for four types of devices with etching times of (a) 0 s, (b) 10 s, (c) 30 s, and (d) 60 s at the RH 30%.

6. Formation voltage of devices with different etching times

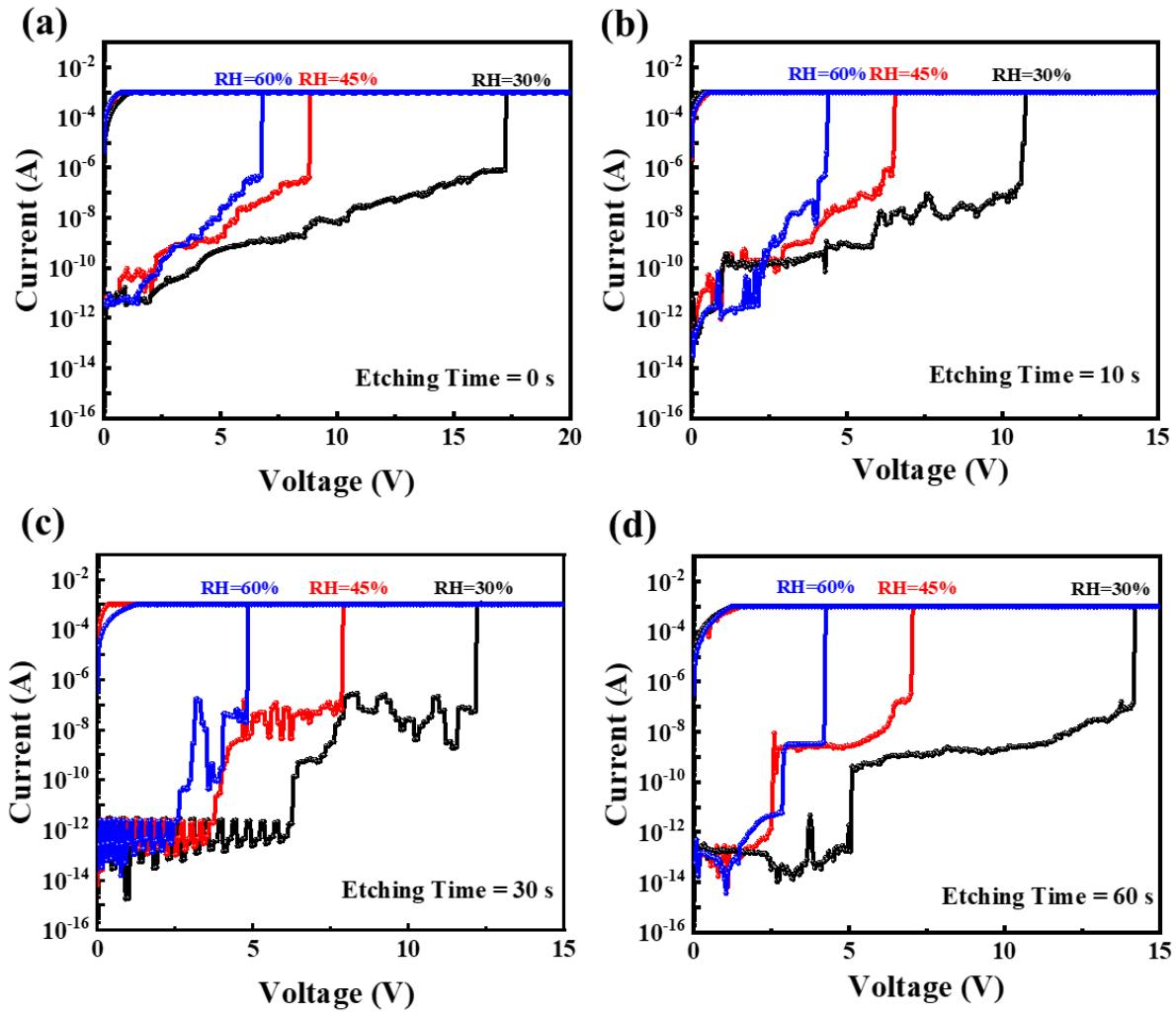

Figure S6. Electroforming curves of SiO_x-based memristors with etching times of (a) 0 s, (b) 10 s, (c) 30 s, and (d) 60 s at different RH.

7. Endurance test of the device with the etching time is 10 s at the range of RH 30%-60%

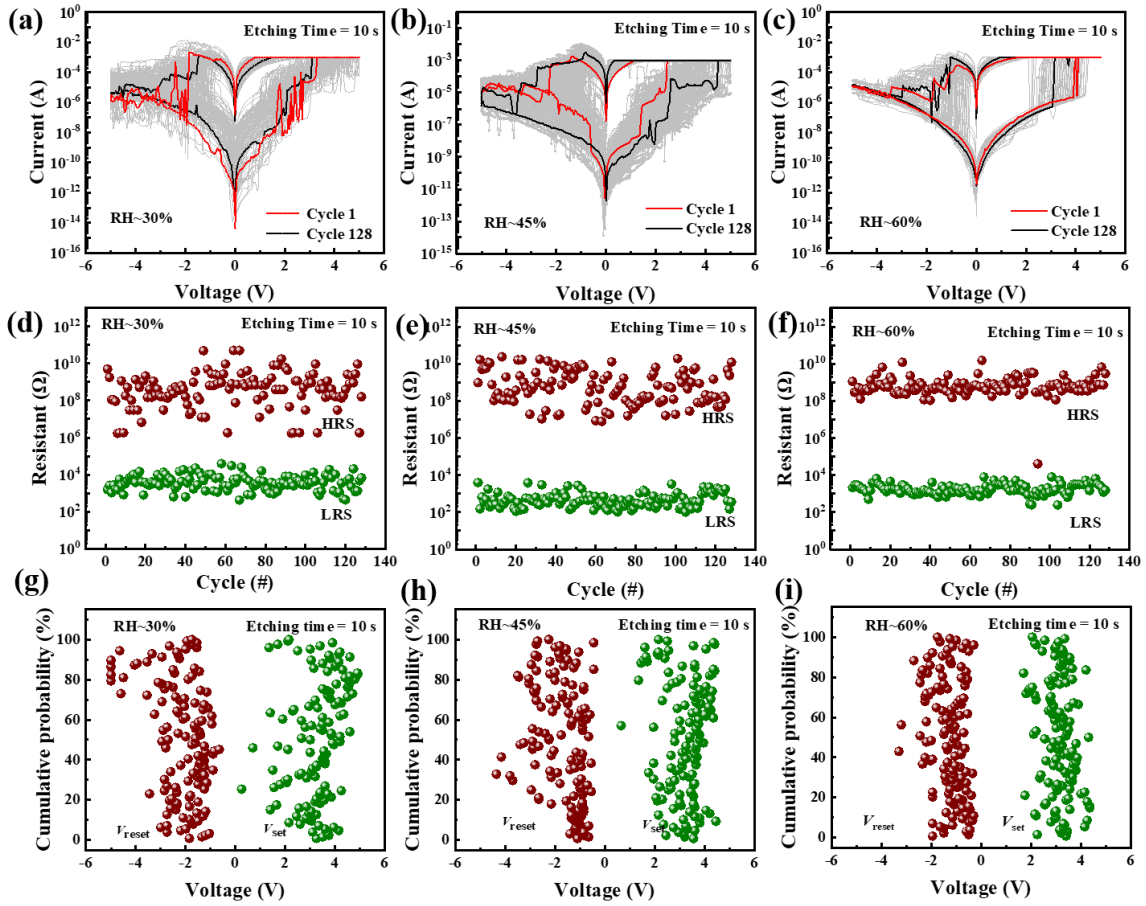

Figure S7. (a)-(c) *I-V* curves of porous SiO_x memristors with different RH range; (d)-(f) Endurance of porous SiO_x memristors with different RH range; (g)-(i) cumulative probability of SET voltage and RESET voltage of porous SiO_x memristors with different RH range.

8. Endurance test of the device with the etching time is 30 s at the range of RH 30%-60%

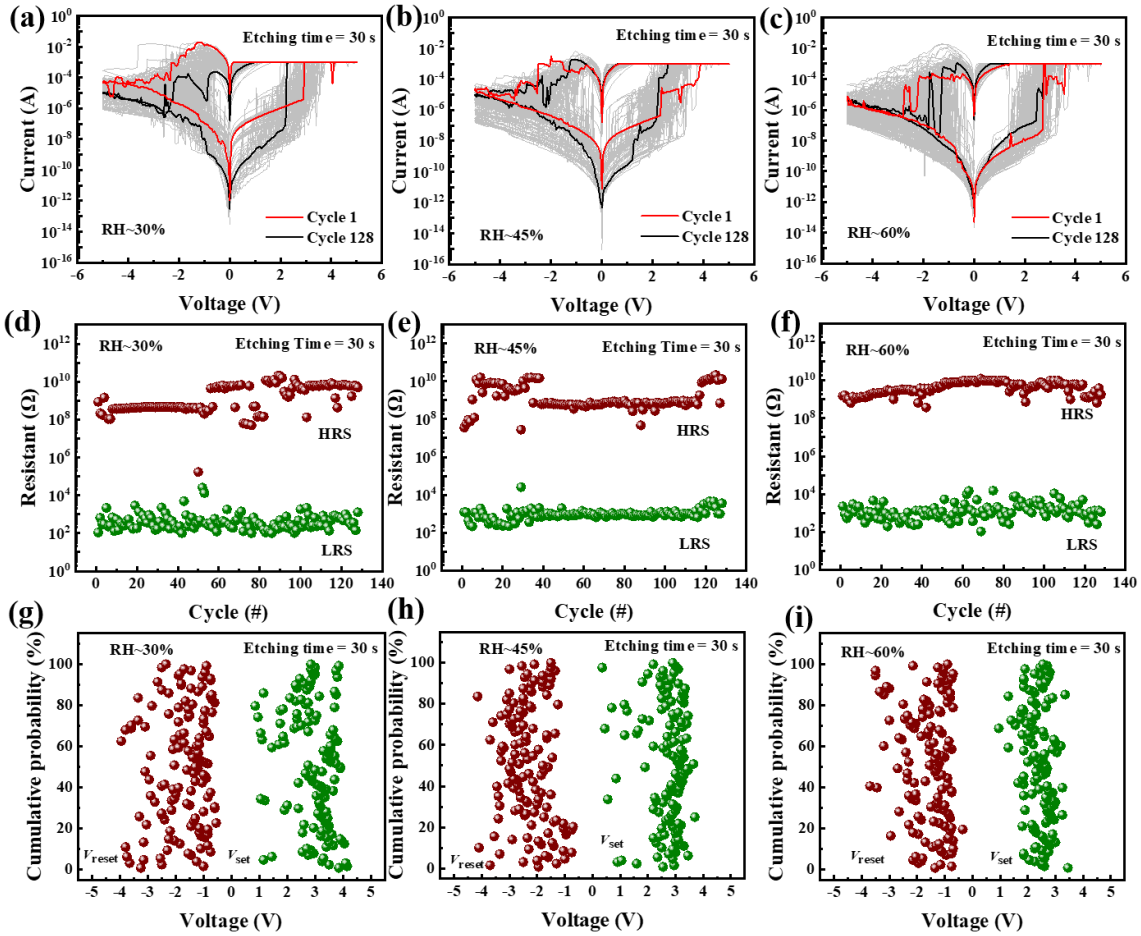

Figure S8. (a)-(c) *I-V* curves of porous SiO_x memristors with different RH range; (d)-(f) Endurance of porous SiO_x memristors with different RH range; (g)-(i) cumulative probability of SET voltage and RESET voltage of porous SiO_x memristors with different RH range.

9. Endurance test of the device with the etching time is 60 s at the range of RH 30%-60%

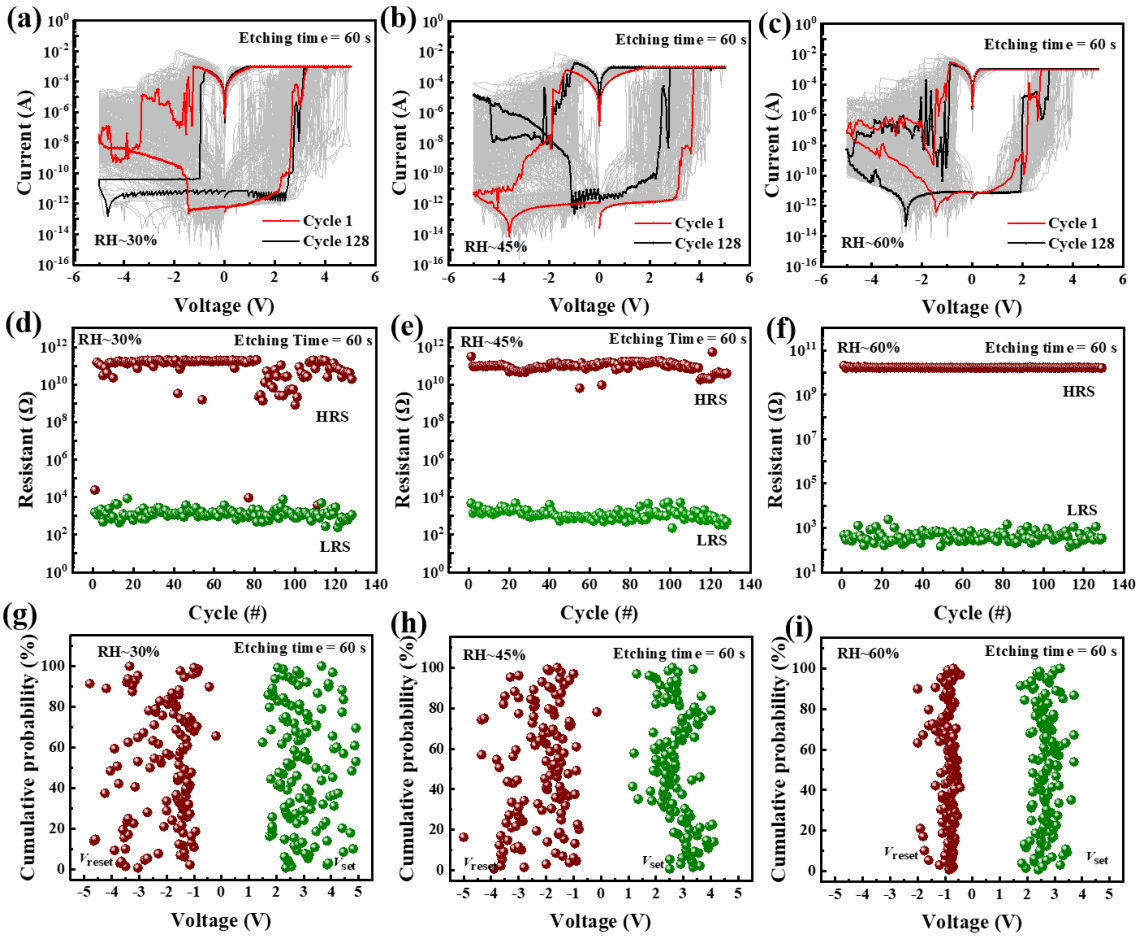

Figure S9. (a)-(c) *I-V* curves of porous SiO_x memristors with different RH range; (d)-(f) Endurance of porous SiO_x memristors with different RH range; (g)-(i) cumulative probability of SET voltage and RESET voltage of porous SiO_x memristors with different RH range.

10. In addition, the on-off ratio of devices in the endurance test for 10^3 cycles. The etching time is 60 s and the RH range of 30%-60%. The positive/negative pulse amplitude is 5 V/-7 V and the pulse period is 20 ms, respectively. The pulse width is 10 ms and the pulse interval is 10 ms, respectively.

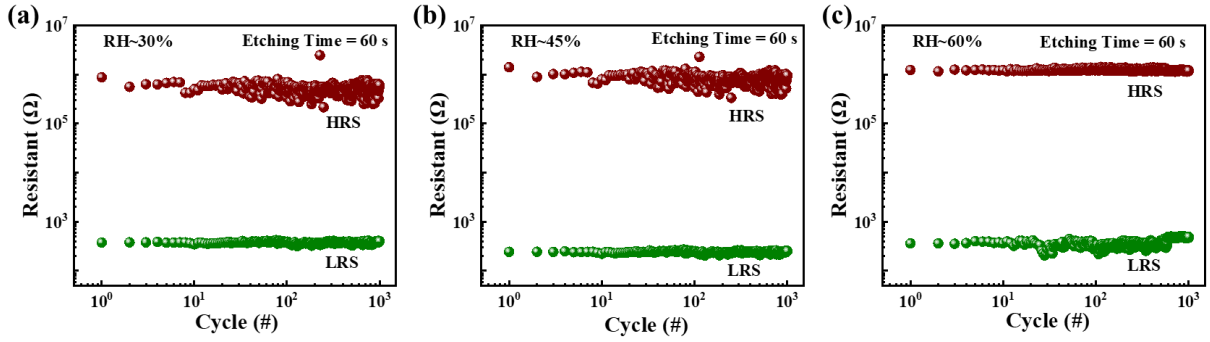

Figure S10. Endurance test of the device with the etching time is 60 s at the range of RH 30%-60%. (a) RH is ~30%, (b) RH is ~45%, (c) RH is ~60%

11. The statistics of voltage and resistance state of devices with etching time 0 s at the RH range of 30%-60%

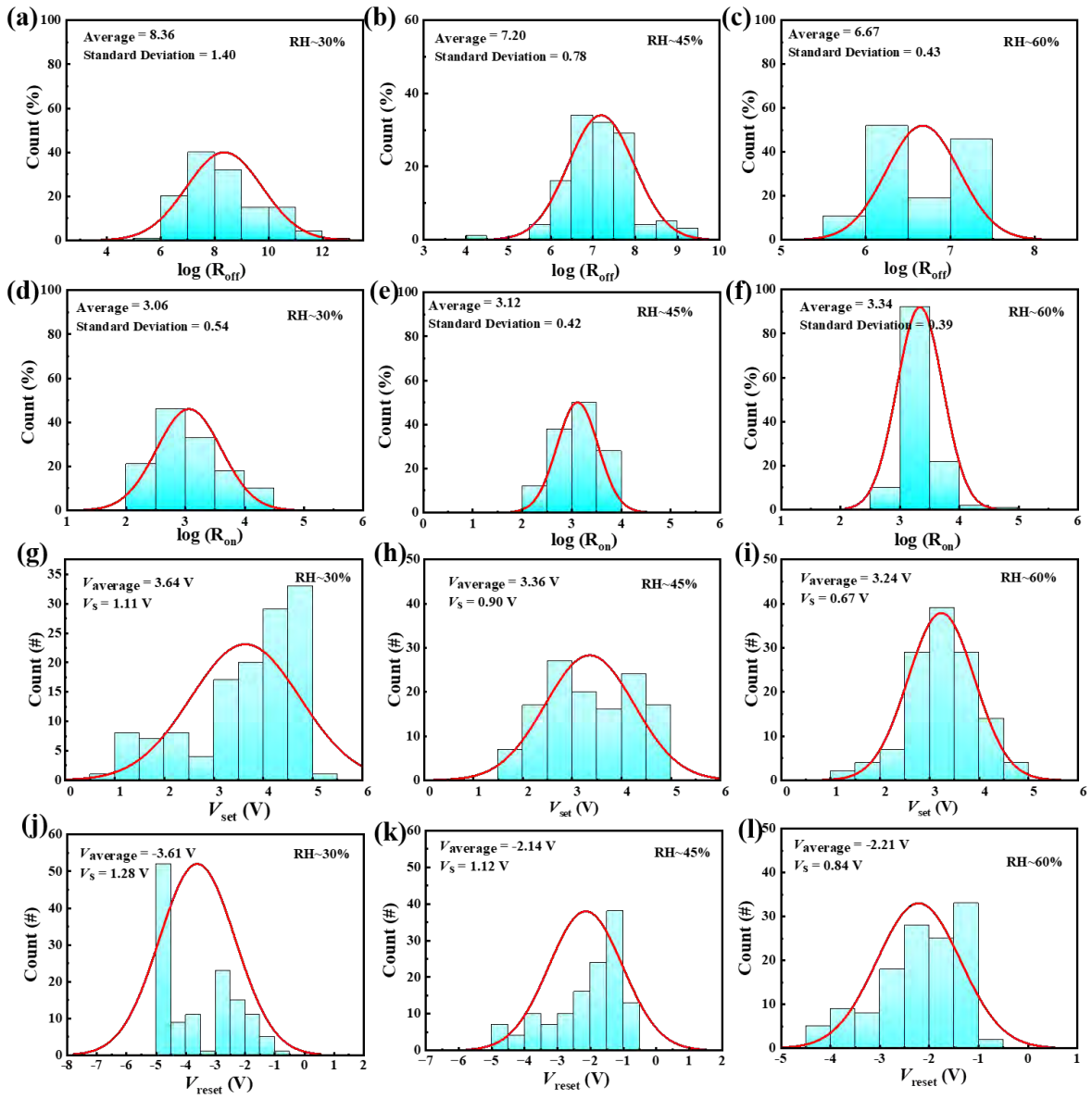

Figure S11. Probability distribution of (a)-(c) log (R_{off}), (d)-(f) log (R_{on}), (g)-(i) SET voltage, (j)-(l) RESET voltage extracted from 128 *I-V* cycles of the device with etching time of 0 s at the RH range of 30%-60%

12. The statistics of voltage and resistance state of devices with etching time 10 s at the RH range of 30%-60%

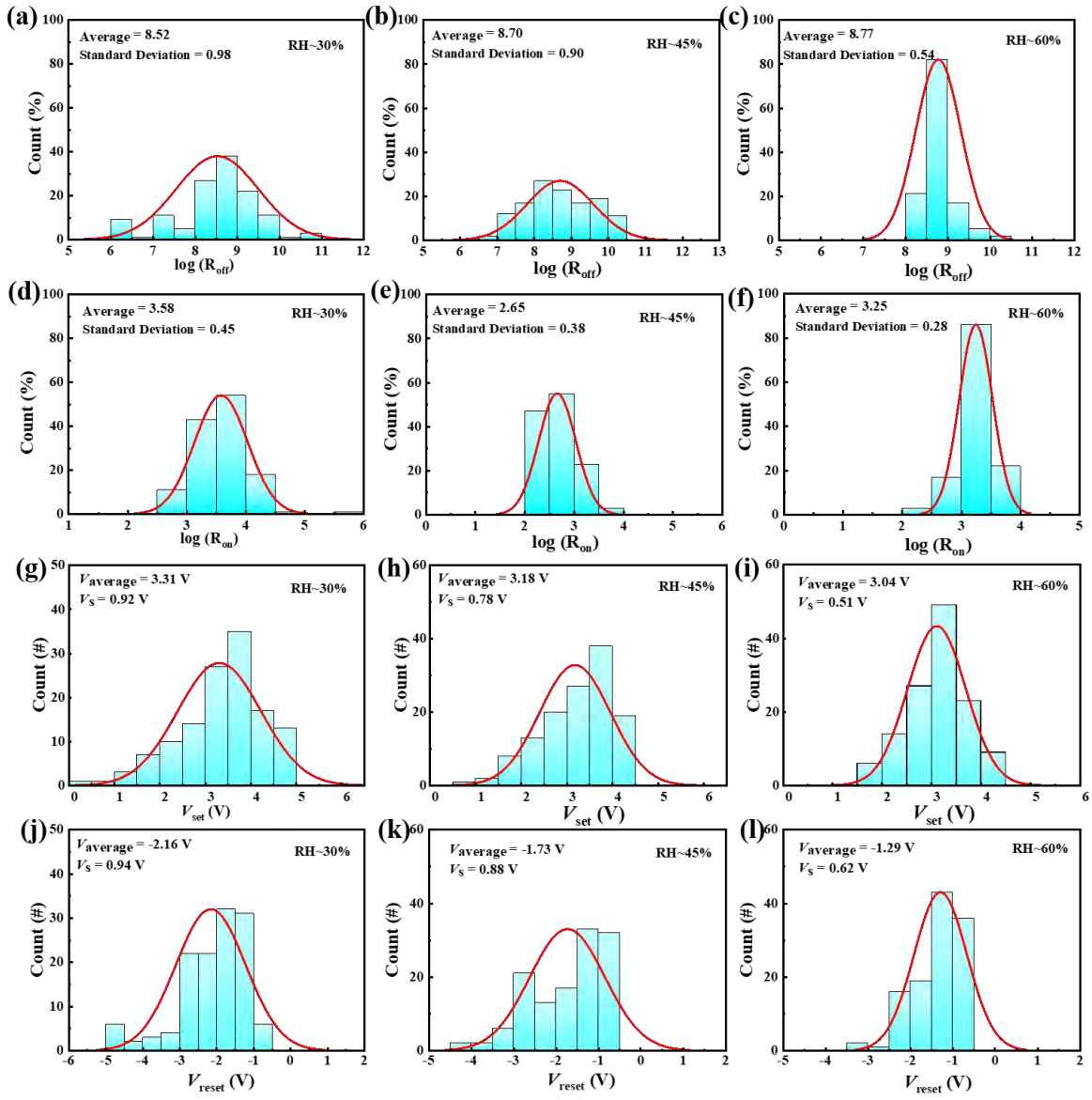

Figure S12. Probability distribution of (a)-(c) log (R_{off}), (d)-(f) log (R_{on}), (g)-(i) SET voltage, (j)-(l) RESET voltage extracted from 128 *I-V* cycles of the device with etching time of 10 s at the RH range of 30%-60%.

13. The statistics of voltage and resistance state of devices with etching time 30 s at the RH range of 30%-60%

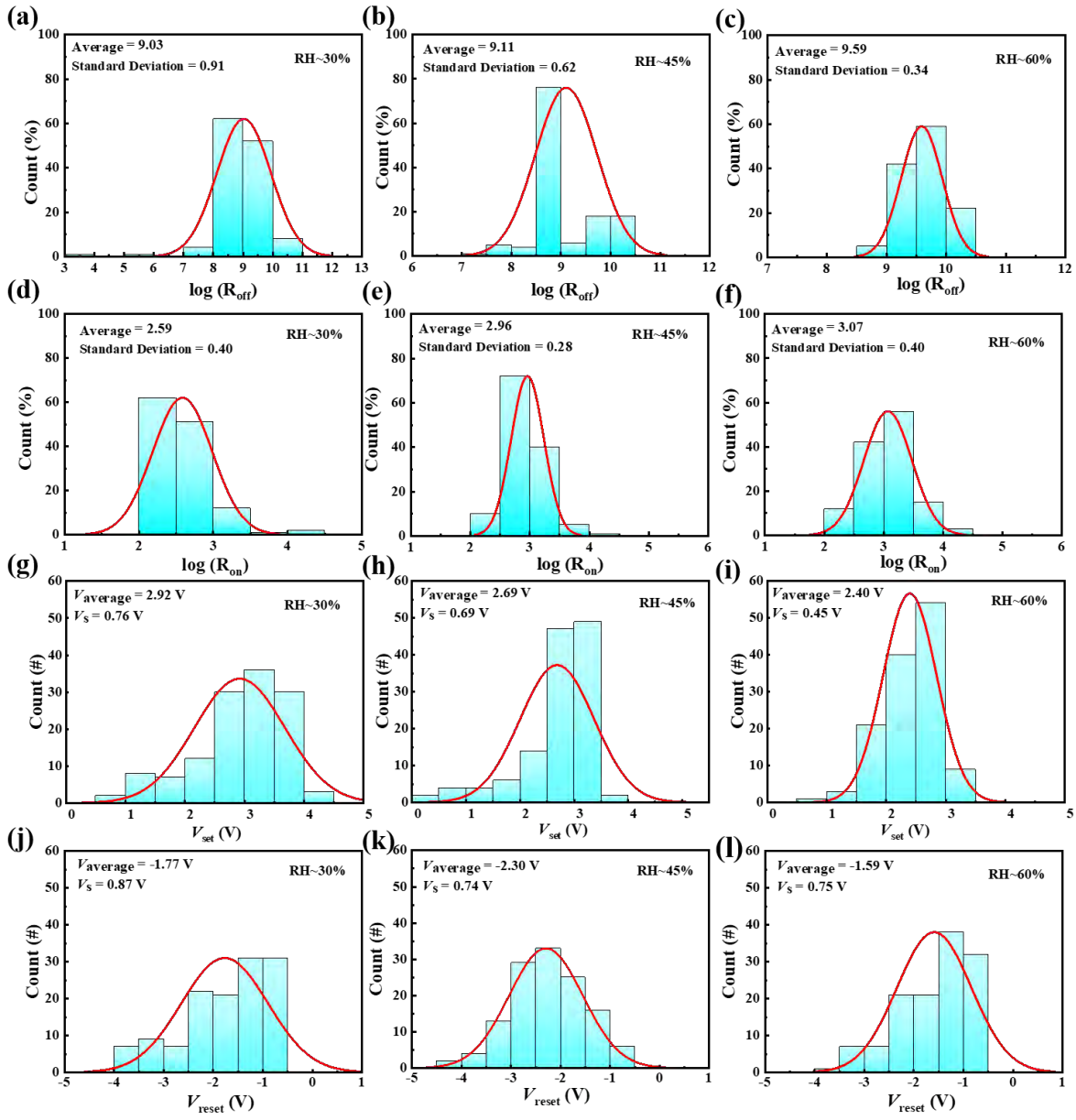

Figure S13. Probability distribution of (a)-(c) log (R_{off}), (d)-(f) log (R_{on}), (g)-(i) SET voltage, (j)-(l) RESET voltage extracted from 128 *I-V* cycles of the device with etching time of 30 s at the RH range of 30%-60%.

14. The statistics of voltage and resistance state of devices with etching time 60 s at the RH range of 30%-60%

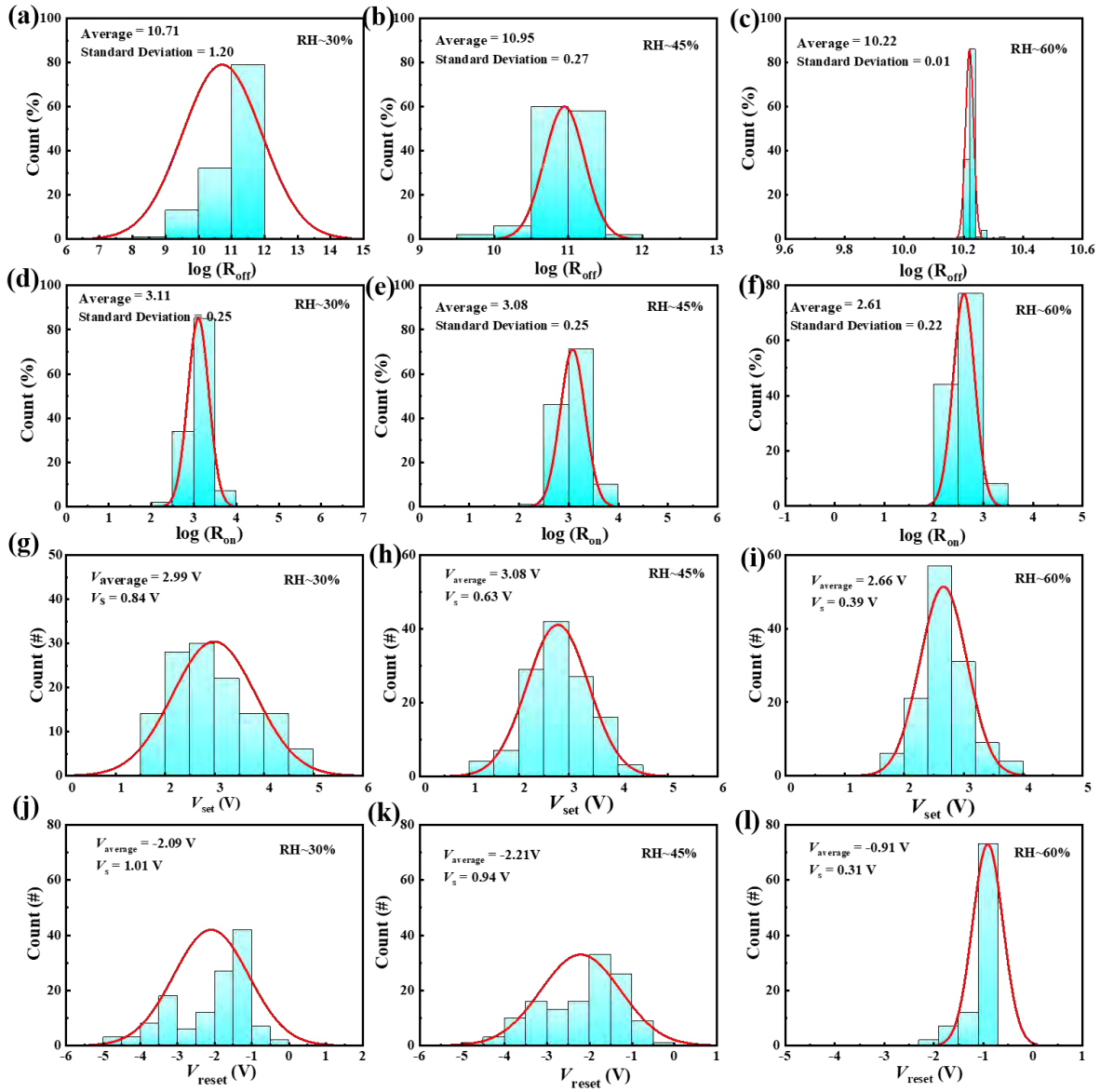

Figure S14. Probability distribution of (a)-(c) log (R_{off}), (d)-(f) log (R_{on}), (g)-(i) SET voltage, (j)-(l) RESET voltage extracted from 128 *I-V* cycles of the device with etching time of 60 s at the RH range of 30%-60%.

15. *I-V* curve of devices with the different etching times at the RH of 75%

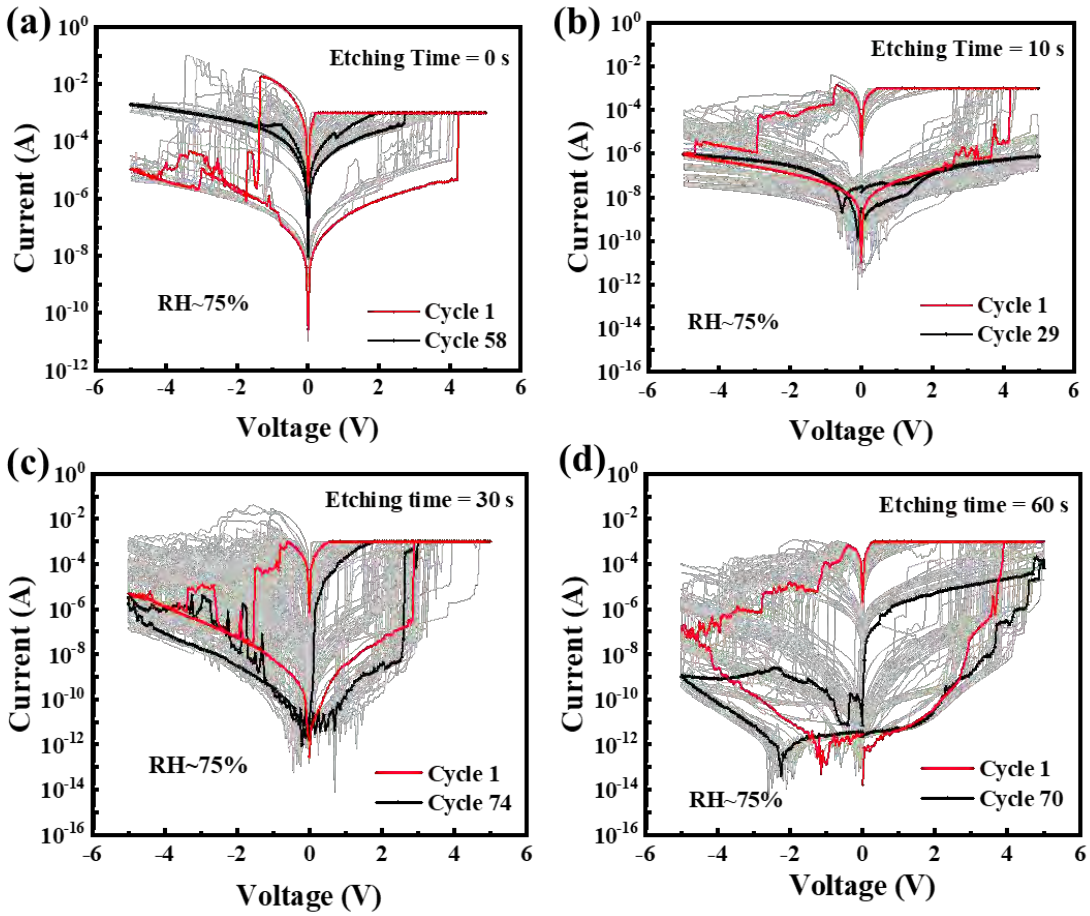

Figure S15. *I-V* curves of devices with etching times of (a) 0 s, (b) 10 s, (c) 30 s and (d) 60 s at RH 75%.

16. Retention characteristics of devices with different etching time at the range of RH 30%-60%

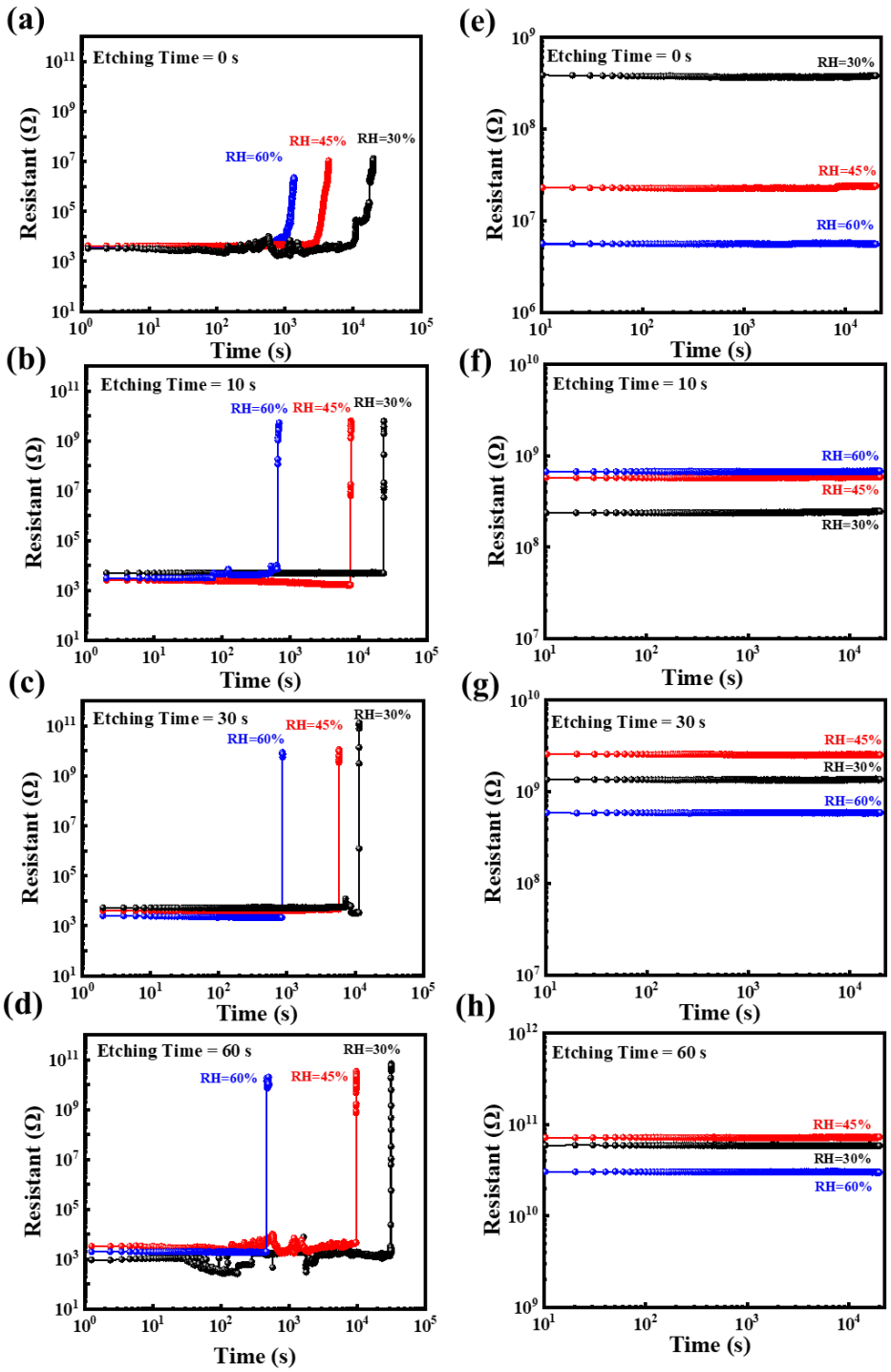

Figure S16. Retention time of devices (a)-(d) LRS and (e)-(h) HRS with different etching times of 0 s, 10 s, 30 s, and 60 s at the range of RH 30%-60%.

17. Compare the performance with other similar devices

Table S1. Summary of memristive performance for various porous-based memristors such as single porous, array porous. The V_{set}, V_{reset}, endurance cycles, on-off ratio and retention are summarized. The symbol "×" means the parameter has not been mentioned in the references.

Structure	V_{set} (V)	V_{reset} (V)	Cycles (#)	on-off	Retention (s)	Refs.
Pt/MLG/single NPTa_2O_{5-x} /Ta/Pt/Ti/SiO_2/Si	8	-8	2000	7.4	×	(2)
Pt/MLG/array NPTa_2O_{5-x} /Ta/Pt/Ti/SiO_2/Si	8	-8	×	~10	5×10^3	(3)
Au/NPSiO_x/Pt	5	15	$\geq 10^5$	~$10^3 - 10^7$	10^4	(4)
Pt/NPSiO_x/Pt	×	×	$\geq 10^5$	~4×10^4	×	(4)
Au/StcNPSiO_x/Pt/Ta	6	-16	$\geq 10^3$	10^3~10^7	10^4	(5)
Ag/porous SiO_2/ITO	~0.47	-3	×	$> 10^2$	2.5×10^3	(6)
Cu/NP WO_{3-x}/ITO	1	-1.1	$\geq 10^3$	10^5	5×10^5	(7)
Pt/Zr:SiO_x/porous SiO_x /TiN/Ti/SiO_2/Si	~0.8	-1.5	100	~10^2	×	(8)
Al/ZnO/ZnO/PSi/Si	1.7	-0.9	100	5.02	×	(9)
Pt/TaO_y/NPTaO_x/Ta	10	-10	5×10^3	~10	1.2×10^4	(10)
Au/$LiCoO_2$/porous SiO_2/Si	3.07	-3.09	300	~10^6	~10^5	(11)
Pt/P$LiCoO_2$/PSiO_2/Si	8	-10	128	~10^8	>>10^5	(12)
Ag/porous silk fibroin/ITO	0.3	-0.2	100	>10	10^4	(13)

Ag/Ag-LTA zeolite/Al	~1.2	-1	50	100	10^4	(14)
Pt/$LiCoO_2$/P-MoS_2 NS/P-SiO_x/Si	4	-5	128	~10^6	10^5	(15)
Ag/$MAPbCl_3$ NWs (AAO)/Al	3	-2.5	~10^6	~10^7	~10^7	(16)
Ag/$MA_3Bi_2I_9$ NWs (AAO)/Al	2.5	-2.1	10^7	10^7	10^4	(17)
ITO/ porous -ITO	-0.02	0.4	100	10	10^3	(18)
Cu/TiO_2/Ti nanopore array	-1.59	1.33	100	70	×	(19)
Ag/porous SiO_x/Si	2.66	-0.91	10^3	~10^8	>>10^4	Our work

18. Physical mechanism analysis of the devices with decreasing retention time with increasing RH

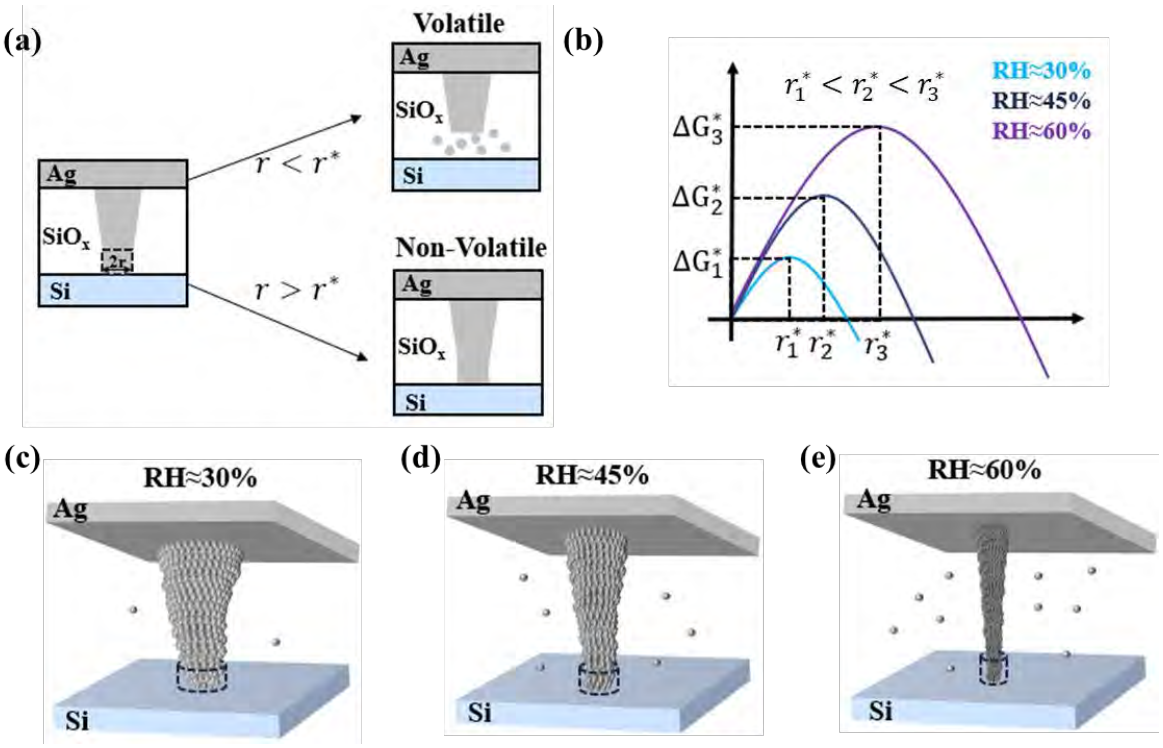

Figure S17. (a) Change process of CF after removing voltage. (b)Influence of different RH on

the relation between Gibbs free energy (G) and the tip of the CF size r with different surface energies (γ_D). Surface atomic diffusion of the conductive filament at (c) RH≈30%, (d) RH≈45%, and (e) RH≈ 60%.[20]

References

(1) Wang, Y.; Zhu, Y.; Li, Y.; Zhang, Y.; Yang, D.; Pi, X. Dual-modal optoelectronic synaptic devices with versatile synaptic plasticity. *Adv. Funct. Mater.* **2022,** *32*, 2107973.

(2) Wang, G.; Lee, J. H.; Yang, Y.; Ruan, G.; Kim, N. D.; Ji, Y.; Tour, J. M. Three-Dimensional Networked Nanoporous Ta_2O_{5-x} Memory System for Ultrahigh Density Storage. *Nano Lett.* **2015**, *15*, 6009-6014.

(3) Kwon, S.; Kim, T. W.; Jang, S.; Lee, J. H.; Kim, N. D.; Ji, Y., Li. C. H.; Tour J. M., Wang, G. Structurally engineered nanoporous Ta_2O_{5-x} selector-less memristor for high uniformity and low power consumption. *ACS Appl. Mater. Interfaces* **2017**, *9*, 34015-34023.

(4) Wang, G.; Yang, Y.; Lee, J. H.; Abramova, V.; Fei, H.; Ruan, G.; Tour, J. M. Nanoporous silicon oxide memory. *Nano Lett.* **2014**, *14*, 4694-4699.

(5) Kwon, S.; Jang, S.; Choi, J. W.; Choi, S.; Jang, S.; Kim, T. W.; Wang, G. Controllable switching filaments prepared via tunable and well-defined single truncated conical nanopore structures for fast and scalable SiO_x memory. *Nano Lett.* **2017**, *17*, 7462-7470.

(6) Zhou, J. Resistive Switching Characteristics of PECVD-Deposited Porous SiO_2-Based Electrochemical Metallisation Memory Cells. *Electron. Lett.* **2016**, *52*, 965-966.

(7) Ji, Y.; Yang, Y.; Lee, S. K.; Ruan, G.; Kim, T. W.; Fei, H.; Lee S.; Kim D.; Yoon J.; Tour, J. M. Flexible nanoporous WO_{3-x} nonvolatile memory device. *ACS Nano* **2016**, *10*, 7598–7603.

(8) Tsai, T. M.; Chang, K. C.; Zhang, R.; Chang, T. C.; Lou, J. C.; Chen, J. H.; Young, T. F.; Tseng, B. H.; Shih, C. C.; Pan, Y. C.; Chen, M. C.; Pan, J. H.; Syu, Y. E.; Simon M.; Sze

Chen, M. C. Performance and Characteristics of Double Layer Porous Silicon Oxide Resistance Random Access Memory. *Appl. Phys. Lett.* **2013**, *102,* 253509.

(9) Martínez, L.; Becerra, D.; Agarwal, V. Dual layer ZnO configuration over nanostructured porous silicon substrate for enhanced memristive switching. *Superlattice Microst.* **2016**, *100*, 89-96.

(10) Choi, S.; Jang, S.; Moon, J. H.; Kim, J. C.; Jeong, H. Y.; Jang, P.; Lee K.; Wang, G. A self-rectifying TaOy/nanoporous TaO_x memristor synaptic array for learning and energy-efficient neuromorphic systems. *NPG Asia Mater.* **2018**, *10*, 1097–1106.

(11) Gao, Q.; Huang, A.; Hu, Q.; Zhang, X.; Chi, Y.; Li, R.; Shi, H.; Chu P. K. Stability and Repeatability of a Karst-like Hierarchical Porous Silicon Oxide-Based Memristor. *ACS Appl. Mater. Interfaces* **2019**, *11*, 21734-21740.

(12) Gao, Q.; Huang, A.; Zhang, J.; Ji, Y.; Zhang, J.; Chen, X.; Geng, X.; Hu, Q.; Wang, M.; Xiao, Z.; Chu, P. K. Artificial synapses with a sponge-like double-layer porous oxide memristor. *NPG Asia Mater.* **2021**, *13*, 1-10.

(13) Wang, J.; Shi, C.; Sushko, M. L.; Lan, J.; Sun, K.; Zhao, J.; Liu, X.; Yan, X.; Boost of the bio-memristor performance for artificial electronic synapses by surface reconstruction. *ACS Appl. Mater. Interfaces* **2021**, *13*, 39641-39651.

(14) Zeng, T.; Zou, X.; Wang, Z.; Yu, G.; Yang, Z.; Rong, H.; Zhang, C.; Xu, H.; Lin, Y.; Zhao, X.; Ma, J.; Zhu, G.; Liu, Y.; Zeolite-Based Memristive Synapse with Ultralow Sub 10 fJ Energy Consumption for Neuromorphic Computation. *Small* **2021**, *17*, 2006662.

(15) Zhang, J.; Ji, Y.; Gao, Q.; Gao, J.; Geng, X.; Li, H.; Shi, H.; Wang, M.; Xiao, Z.; Chu, P. K.; Huang, A. Artificial Synapse Based on Bio-Hierarchical Porous Memristor Driven by

Multilevel-Ions Migration. *Adv. Electron. Mater.* **2022**, *8*, 2200269.

(16) Zhang, Y.; Poddar, S.; Huang, H.; Gu, L.; Zhang, Q.; Zhou, Y.; Yan, S.; Zhang, S.; Song, Z.; Huang, B.; Shen, G.; Fan, Z. Three-dimensional perovskite nanowire array–based ultrafast resistive RAM with ultralong data retention. *Sci. Adv.* **2021**,*7*, eabg3788.

(17) Poddar, S.; Zhang, Y.; Chen, Z.; Ma, Z.; Fu, Y.; Ding, Y.; Chan, C. L. J.; Zhang, Q.; Zhang, D.; Song, Z.; Fan, Z. Image processing with a multi-level ultra-fast three dimensionally integrated perovskite nanowire array. *Nanoscale Horiz.* **2022**, *7*, 759-769.

(18) Wang, Y.; Hu, L.; Wei, X.; Zhuge, F. Ultralow operation voltages of a transparent memristor based on bilayer ITO. *Appl. Phys. Lett.* **2020**, *116*, 0008416.

(19) Tao, D.; Jiang, Z.; Chen, J.; Qi, B.; Zhang, K.; Wang, C. Stable resistive switching characteristics from highly ordered Cu/TiO_2/Ti nanopore array membrane memristors. *Appl. Surf. Sci.* **2021**, *539*, 148161.

(20) Ding, X.; Huang, P.; Zhao, Y.; Feng, Y.; Liu, L. Understanding of the volatile and nonvolatile switching in Ag-based memristors. *IEEE Trans. Electron Devices* **2022,** *69*, 1034-1040.